

Integrating brain and biomechanical models - a new paradigm for understanding neuro-muscular control

Sebastian James^{1,2,*}, Chris Papapavlou⁵, Alexander Blenkinsop^{1,2},

Alexander Cope³,

Sean Anderson^{2,4}, Konstantinos Moustakas⁵, Kevin Gurney^{1,2}

¹ Adaptive Behaviour Research Group, Department of Psychology, The University of Sheffield, Sheffield, UK

² Insigneo Institute for *in-silico* Medicine, The University of Sheffield, Sheffield, UK

³ Department of Computer Science, The University of Sheffield, Sheffield, UK

⁴ Department of Automatic Control Systems Engineering, The University of Sheffield, Sheffield, UK

⁵ Department of Electrical and Computer Engineering, The University of Patras, Patras, Greece

Correspondence*:

Kevin Gurney

Department of Psychology, The University of Sheffield, Western Bank, Sheffield, S10 2TP, UK, k.gurney@sheffield.ac.uk

2 ABSTRACT

To date, realistic models of how the central nervous system governs behaviour have been restricted in scope to the brain, brainstem or spinal column, as if these existed as disembodied organs. Further, the model is often exercised in relation to an *in vivo* physiological experiment with input comprising an impulse, a periodic signal or constant activation, and output as a pattern of neural activity in one or more neural populations. Any link to behaviour is inferred only indirectly via these activity patterns. We argue that to discover the principles of operation of neural systems, it is necessary to express their behaviour in terms of physical movements of a realistic motor system, and to supply inputs that mimic sensory experience. To do this with confidence, we must connect our brain models to neuro-muscular models and provide relevant visual and proprioceptive feedback signals, thereby closing the loop of the simulation. This paper describes an effort to develop just such an integrated brain and biomechanical system using a number of pre-existing models. It describes a model of the saccadic oculomotor system incorporating a neuromuscular model of the eye and its six extraocular muscles. The position of the eye determines how illumination of a retinotopic input population projects information about the location of a saccade target into the system. A pre-existing saccadic burst generator model was incorporated into the system, which generated motoneuron activity patterns suitable for driving the biomechanical eye. The model was demonstrated to make accurate saccades to a target luminance under a set of environmental constraints. Challenges encountered in the development of this model showed the importance of this integrated modelling approach. Thus, we exposed shortcomings in individual model components which were only apparent when these

were supplied with the more plausible inputs available in a closed loop design. Consequently we were able to suggest missing functionality which the system would require to reproduce more realistic behaviour. The construction of such closed-loop animal models constitutes a new paradigm of *computational neurobehaviour* and promises a more thoroughgoing approach to our understanding of the brain's function as a controller for movement and behaviour.

Keywords: integrated brain biomechanics neuromuscular oculomotor saccade basal ganglia

1 INTRODUCTION

The field of computational neuroscience has provided many *systems models* of the brain (Arai et al., 1994; Gancarz and Grossberg, 1998; Hazy et al., 2007; Blenkinsop et al., 2017). We refer to these as *mechanistic computational models*, meaning models which consist of populations of neural elements, interconnected in a biologically plausible manner, which simulate the operation of the brain. Whilst they differ in scale and complexity, these models all seek to describe the fundamental mechanisms behind common animal behaviours such as locomotion, threat evasion, reaching or feeding. However, none of the models cited here actually reproduce these behaviours. In each case, the activity in a certain population of neurons is taken to be representative of a behavioural outcome. In some cases, it is reasonable to take the activity of an internal population within the brain model as being representative of the induced behaviour. For example, a choice made in a *go/no-go* task could be determined from activity in a population within a basal ganglia model (Nambu et al., 1990; Khn et al., 2004). The decision to *go* is selected by a reduction of activity in this population; maintenance of activity implies *no-go*. To validate the model, the error rates which it generates could be compared with experimentally determined error rates in primate subjects. We refer to this as an *output assumption model* because the output is assumed to signify behaviour. (An *input assumption model* assumes that sensory input produces some particular form of neural activity in an input population of the model.)

However, we may be interested in reproducing accurate simulated *trajectories*, in order to find out how degradation of parts of the model affect movement. In Parkinson's Disease, degradation of the dopamine neurons originating in the substantia nigra pars compacta (SNc) causes dyskinesia (Galvan and Wichmann, 2008), as well as abnormal network activity in the basal ganglia (Brown et al., 2001; McCarthy et al., 2011). Sufferers of the disease would be expected to produce abnormal decision-making *and* movement trajectories in a reach-to-the-correct-target task such as the one described in James et al. (2017). A model which sought to explore in detail the effects of the SNc degradation both on the decision making *and* on the movement dynamics would need a physically accurate virtual arm, as well as physically realistic sensory input for the brain. This is no less than a complete model of those sections of the brain and body which act to fulfil the task. Such a modelling effort, if successful, would result in a virtual robot capable of expressing behaviour *in response to sensory input from its environment*. This would represent a paradigm shift in the field of computational neuroscience worthy of the new name of *computational neurobehaviour*.

In an attempt to build a model combining brain, realistic biomechanics *and* sensory feedback, we sought to extend our previous work modelling the oculomotor system. The existing model (Cope et al., 2017) is already able to capture sensory input and convert it into a neural signal, assumed to specify the target of a *saccadic eye movement*; a fast movement of the eyes which directs the fovea to a region of interest in the field of view. The oculomotor system is an excellent candidate for modelling because its movements can be specified with only three degrees of freedom, making it one of the simplest neuro-muscular system in the body. It is nevertheless behaviourally interesting, as saccadic eye movements reveal information about

64 decision making at a subconscious level (Deubel and Schneider, 1996; Reppert et al., 2015; Marcos and
65 Genovesio, 2016). The modelling of the oculomotor system is served by a large body of behavioural data
66 describing saccades (Tipper et al., 2001; Walker et al., 1997; Casteau and Vitu, 2012), many anatomical
67 studies of the neural substrates involved (Meredith and Ramoa, 1998; Isa, 2002; Isa and Hall, 2009) and
68 electrophysiological data linking these together (Hepp and Henn, 1983; Dorris et al., 1997; McPeek et al.,
69 2003; Vokoun et al., 2011). Furthermore, in the context of building *behaving* systems a necessary part of
70 any model for which the behaviour requires visual attention and decision making is a realistic mechanism
71 for gathering visual information. This is obvious from extrinsic considerations—a subject must look at a
72 scene to make decisions or navigate within it. It also follows for *intrinsic* reasons. For example, Howard
73 and Tipper (1997) showed that visual cues affect reach trajectories and the same group later demonstrated
74 that reaching affects the saccadic system (Tipper et al., 2001) suggesting a close relationship between
75 these neural systems. Building the simplest, behaving oculomotor system will therefore assist future
76 computational neurobehavioural modelling efforts.

77 Many neural populations are involved in the coding of saccadic eye movements, only a very brief overview
78 is given here; for a review, see Munoz (2002). One pathway takes information from the retina directly
79 into the superficial layers of the superior colliculus in the brainstem (Sterling, 1971; Linden and Perry,
80 1983; Wu et al., 1994). Activity within the superior colliculus then excites neurons in the pons, medulla
81 and rostral mid-brain (Sparks, 2002) and then through channels to the motor neurons which innervate the
82 extraocular muscles (Fuchs and Luschei, 1970; Sparks, 2002). This direct pathway is responsible for the
83 low latency saccades called express saccades (Schiller et al., 1987; Edelman and Keller, 1996). Information
84 from the retina is also processed by visual cortex which feeds through to the frontal eye fields in which
85 activity is related to reflexive and voluntary saccades (Schall and Thompson, 1999). Activity build-up in the
86 frontal eye fields is transferred to the intermediate layers of the superior colliculus (Stanton et al., 1988b)
87 and is also processed by the basal ganglia, which participates in the selection of the winning saccade end
88 point (Stanton et al., 1988a). Although both cortical and subcortical paths produce a saccade target signal
89 in the superior colliculus, it is also possible for animals to make relatively normal saccades even after the
90 colliculus has been ablated (Wurtz and Goldberg, 1972; Aizawa and Wurtz, 1998), though express saccades
91 are lost with collicular lesions (Schiller et al., 1987). This makes the superior colliculus a perplexing
92 structure, being both critically involved in saccade target specification (Sparks and Nelson, 1987) and
93 saccade dynamic control (Waitzman et al., 1991; Goossens and Van Opstal, 2012) and yet dispensable.
94 The ‘backup pathway’ likely incorporates the oculomotor vermis and fastigial oculomotor region of the
95 cerebellum which are known to participate in the specification, dynamics and adaptation of saccadic eye
96 movements (Kleine, 2003; Takagi et al., 1998).

97 There is a long history of modelling the oculomotor system. For a comprehensive review, see Girard
98 and Berthoz (2005). Models of individual systems have been proposed for brainstem (Robinson, 1975;
99 Scudder, 1988; Gancarz and Grossberg, 1998), cerebellum (Quaia et al., 1999; Dean, 1995; Dean et al.,
100 1994) and superior colliculus (Arai et al., 1994; Morn et al., 2013; Marino et al., 2012). More recently,
101 combined models have also been developed incorporating sensory input (Cope et al., 2017) and driving
102 simple physical plants representing the eye (Tabareau et al., 2007; N’Guyen et al., 2014; Thurat et al.,
103 2015). None of these models has yet fully closed the loop to produce a behaving system operating freely
104 within its environment. We argue that developing integrated, closed-loop models of behaving systems
105 offers insights into the operation of neural systems that are not available from input- or output-assumption
106 models.

2 MATERIAL & METHODS

107 The integrated brain and biomechanical model described here is a development of the model in Cope
108 et al. (2017), referred to here as the Cope-Chambers-Prescott-Gurney model. This was a rate-coded neural
109 network model incorporating retinal populations, frontal eye fields (FEF), the basal ganglia (BG), and the
110 superior colliculus (SC). In the Cope-Chambers-Prescott-Gurney model, the centroid of the activity in the
111 deep layers of superior colliculus was assumed to accurately encode the location of the eye at the end of the
112 saccade (Wurtz and Goldberg, 1972; Robinson, 1972; Van Gisbergen et al., 1987; McIlwain, 1982). This
113 location was used to recalculate the positions of the luminances in the eye's frame of reference at each time
114 step. The model included no brainstem populations other than superior colliculus, nor a neuromuscular
115 model.

116 To summarize, the Cope-Chambers-Prescott-Gurney model takes as *input* the positions of luminances on
117 a topographic map and produces as output a saccade target.

118 To the Cope-Chambers-Prescott-Gurney model, we added a rate-coded brainstem model (a 'saccadic
119 burst generator') and a biomechanical eye, implemented using the biomechanical modelling framework
120 OpenSim. These will be described below, but first we will give a description of the co-ordinate systems and
121 the modelling framework used.

122 2.0.1 Co-ordinates in the world

123 Before describing the biomechanical eye and the brain model, which consisted of retinotopically mapped
124 neural sheets, we describe the co-ordinate system used in the world. The eye was located at the origin of a
125 three-dimensional, right-handed Cartesian co-ordinate system, with its fovea directed in the $-z$ direction.
126 There was a notional spherical screen which was also centred at the origin of the co-ordinate system and
127 had a radius of 50 (in arbitrary units). The *fixation point* was the point on the screen at which the eye
128 was initially directed. Onto the screen were projected target luminances, each of which having a position
129 described by two co-ordinates; θ_x^t , a rotation of the horizon plane about the x axis, and θ_y^t , a rotation of the
130 meridian plane about the y axis. The position is the intersection of these rotated planes with the spherical
131 screen (disregarding the intersection point of these three surfaces behind the eye). Note that a luminance
132 with positive θ_x^t was above the horizon of this world; one whose θ_y^t was positive lay to the left of the
133 world's meridian. For this reason, many of the figures in this paper are plotted with $-\theta_y$ on the x -axis and
134 θ_x on the y -axis so that targets that lay up and to the right in the world do so in the graphs, also.

135 Luminances were crosses of height and width subtending $\pm 3^\circ$ and whose 'bars' were 2° thick. Lumi-
136 nances were oriented like + symbols with their vertical bar aligned with the meridian plane and their
137 horizontal bar aligned with the horizon.

138 The eye's frame of reference was initially aligned with the world's frame of reference. At each timestep,
139 the eye's rotational state (described by the Euler rotations θ_x , θ_y , θ_z) was used to translate the three
140 dimensional Cartesian co-ordinates of the luminances in the world frame into co-ordinates in the eye frame.
141 The luminance co-ordinates in the eye's frame of reference were used to determine the input to the brain
142 model.

143 2.1 Model development framework

144 The Cope-Chambers-Prescott-Gurney model was originally developed to run on the BRAHMS model
145 execution framework (Mitchinson et al., 2010; Mitchinson and James, 2015). To run a BRAHMS model, the
146 researcher must develop *BRAHMS components* for the various neural elements. A BRAHMS component is

147 a programmatically coded implementation of the behaviour of the component. It may have an arbitrary
148 number of inputs and outputs and may be written in C, C++, Python or MATLAB. The Cope-Chambers-
149 Prescott-Gurney model's components were hand written in C++ and MATLAB. A BRAHMS *SystemML* file
150 describes how the different components connect together and how data is passed between them (Mitchinson
151 et al., 2010). The main BRAHMS program first reads the SystemML file, then dynamically loads all the
152 required components before executing the system.

153 In the current work, the Cope-Chambers-Prescott-Gurney model was reproduced using the declarative
154 SpineML markup language (Alex Cope and Paul Richmond, 2014; Richmond et al., 2014), with the help
155 of the graphical SpineML model editing software called SpineCreator (Cope et al., 2015, 2016). SpineML,
156 which is a development of the NineML specification (INCF Task Force on Multi-Scale Modeling, 2011),
157 describes neural populations and their projections in a highly structured format in which neuron bodies, pre-
158 and post-synapses are described in terms of *SpineML components*. These are similar to the components
159 provided by BRAHMS, but in this case, the components are an XML description of the functionality
160 of the component, rather than a programmatic implementation, with one XML file per component. A
161 SpineML *network layer* file then describes which components are used in the model, and how they are
162 connected together. Finally, a number of SpineML *experiment layer* files specify how the model described
163 in the network layer can be executed. In the experiment layer, the execution duration and timestep can be
164 specified, along with input conditions, connection lesions and component parameter updates. A description
165 of SpineML is given in Richmond et al. (2014); the definitive definition is found in the schemas (Cope
166 et al., 2014). SpineCreator, in its rôle as a graphical editor for the SpineML format, was used to generate
167 the SpineML files describing the model. It was also used to generate the diagrams of the model.

168 As a declarative format for model specification, SpineML is agnostic about how the model is executed. A
169 number of simulation engines can be utilised, including DAMSON (Richmond, 2015), GeNN (Nowotny,
170 2011; Nowotny et al., 2014) and BRAHMS (used here). The simulation engine incorporating BRAHMS is
171 called SpineML_2_BRAHMS (Cope and James, 2015). SpineML_2_BRAHMS is a collection of XSLT
172 stylesheets which first generate and compile C++ BRAHMS components from the SpineML component
173 layer description files. SpineML_2_BRAHMS then uses the SpineML network and experiment layer files
174 to generate a BRAHMS SystemML description of the model. Finally, SpineML_2_BRAHMS executes the
175 model, now described entirely as a BRAHMS system, via a call to the BRAHMS binary. A number of
176 additional hand-written components are present in SpineML_2_BRAHMS providing the inputs (constant
177 inputs, time-varying inputs, etc) which the modeller specifies in the experiment layer.

178 In addition to the brain model components, all of which are code-generated using SpineML_2_BRAHMS as
179 described above, two hand-written components are integrated into the model: The biomechanical eye model
180 and a sensory input component. The sensory input component takes the eye's rotational state and the state
181 of the experimental luminances and projects a retinotopic activity map into the brain model. Both of these
182 BRAHMS components were hand-written in C++. To incorporate these components into the SpineML
183 model, a SpineML_2_BRAHMS *external.xsl* file was used. The external.xsl file scheme for incorporating
184 external BRAHMS components into a SpineML model was a new SpineML_2_BRAHMS feature motivated
185 by the current work. Fig. 1 shows the workflow, in which the model specification files (blue box - a
186 combination of SpineML files and C++ code), are processed (green box) into a BRAHMS system (red
187 box).

188 **2.2 Existing brain model**

189 The brain model, excluding the brainstem, is a re-implementation of the Cope-Chambers-Prescott-
 190 Gurney model. Fig. 2 shows the layout of the populations and the interconnections between them. Each
 191 population of 2500 elements is arranged as a 50 by 50 grid which forms a map in a retinotopic co-ordinate
 192 system, roughly matching the known layout of the superior colliculus (Robinson, 1972).

193 **2.2.1 Components**

194 With the exceptions of the World and FEF_add_noise populations, each neural element represents an
 195 activation; the activation is governed by a first order differential equation specified in the SpineML
 196 component. In the brain model, there are six different components in use: LINlinear; LINret; LINexp;
 197 D1MSN and D2MSN.

198 The LINlinear component governs the activation a with a first order leaky integrator differential equation:

$$\dot{a} = \frac{1}{\tau}(a_{in} - a) \quad (1)$$

199 where τ is the time constant for the neural activation and a_{in} is the input to the neural element. a_{in} is
 200 defined by an activation input and a shunting inhibition input according to:

$$a_{in} = A(1 - s_a) + \alpha R_N \quad (2)$$

201 Here, A is the activation input and s_a is the shunting inhibition state variable whose value is related to the
 202 shunting input, S by

$$s_a = \begin{cases} S & S \leq 1 \\ 1 & S > 1 \end{cases} \quad (3)$$

203 R_N is a random number drawn from a standard normal distribution ($\sigma=1$, $\mu=0$) and introduces noise to the
 204 activation of the neural element, with the parameter α controlling the noise amplitude.

205 The output, y , of LINlinear is related to the activation a by the piecewise linear transfer function

$$y(a) = \begin{cases} 0 & a < c \\ a - c & c \leq a \leq 1 + c \\ 1 & a > 1 + c \end{cases} \quad (4)$$

206 where c is a parameter defining the slope of the transfer function. At this point, the naming scheme for the
 207 component becomes apparent; this is a Leaky Integrator with a piecewise-linear transfer function.

208 The LINret component used for the retinal populations is similar to the LINlinear component, but with
 209 no intrinsic noise and no shunting inhibitory input. It has a neural input which is identical to the activation
 210 input A :

$$a_{in} = A \quad (5)$$

211 The LINexp component is a leaky integrator with an exponential transfer function. It shares the same
 212 differential equation with LINlinear, but has a different input equation and a different output transfer
 213 function. It has the following equation for the neural element input a_{in} :

$$a_{in} = [A + N(a - V_r^-)](1 - S) + 0.01R_N \quad (6)$$

214 where A is the activation input and N is an input which is modulated by V_r^- , a reversal potential, and
 215 a , the current activation of the element. These inputs are summed and then reduced by a factor which
 216 is dependent on S , the shunting input. As in LINlinear, R_N introduces normally distributed noise to the
 217 element.

218 The output, y , of the LINexp component is given by

$$y(a) = \begin{cases} e^a - 0.9 & e^a \leq 1 + 0.9 \\ 1 & e^a > 1 + 0.9 \end{cases} \quad (7)$$

219 This component is used in the subthalamic nucleus (STN) population, as it gives a more physiologically
 220 accurate f-I behaviour (Wilson, 2004; Bevan and Wilson, 1999; Hallworth et al., 2003) which has been
 221 shown to allow the mapping of the basal ganglia network architecture onto an optimal decision making
 222 model (Bogacz and Gurney, 2007).

223 The D1MSN and D2MSN components are both leaky integrators, similar to LINlinear. They differ in
 224 that they have no shunting inhibition. They are used in to model medium spiny neuron (MSN) populations
 225 in the striatum. As they model the fact that most MSN neurons fall into two groups; those expressing D1
 226 dopamine receptors and those expressing D2 receptors, they have a dopamine parameter that modulates the
 227 input activation, so that their equations for a_{in} are thus:

$$a_{in}^{D1} = (0.2 + d)A + 0.01R_N \quad (8)$$

$$a_{in}^{D2} = (1 - d)A + 0.01R_N \quad (9)$$

228 where d is the dopamine parameter. Varying dopamine from 0 to 1 enhances the activation in the D1 model,
 229 whereas it decreases the activation of the D2 model elements, in line with experimental observations
 230 (Harsing and Zigmond, 1997; Gonon, 1997). Note that the equation for a_{in}^{D1} differs from that used in the
 231 Cope-Chambers-Prescott-Gurney model, for which the cortico-striatal weights are multiplied by $(1 + d)$
 232 rather than $(0.2 + d)$.

233 The equations given above are applied to each element in a population. The value of the activation A (and
 234 where relevant, the shunting input, S) is determined by summing the weighted inputs to the population:

$$A = \sum_i w_i^{act} x_i^{act} \quad (10)$$

$$S = \sum_i w_i^{sh} x_i^{sh} \quad (11)$$

235 w_i^{act} and w_i^{sh} are, respectively, the weights of the i^{th} activation or shunting connection; x_i^{act} and x_i^{sh} are
 236 the signals input to the activation and shunting connections.

237 2.2.2 Population activity and retinotopic mapping

238 Each population of 2500 neural elements was arranged in a 50 by 50 grid, with positions on the grid
 239 representing a retinotopic mapping similar to that found empirically both in the superior colliculus (Ottos
 240 et al., 1986) and in visual cortex (Schwartz, 1980) and assumed in this work to persist throughout the
 241 oculomotor system.

244 In a retinotopic mapping, the Cartesian co-ordinates of the light-sensitive cells in the retina, whose density
 245 varies with distance from the fovea, are transformed into the Cartesian co-ordinates of the correspondingly
 246 active cells on the colliculus. The mapping ensures that an even density of cells can be maintained in the
 247 colliculus, but ensures that a group of adjoining, active, retinal neurons will always activate an adjoining
 248 group of neurons on the collicular surface.

249 The mapping turns out to resemble polar co-ordinates. That is, one axis of the collicular surface specifies
 250 the eccentricity of a retinal location (how far it is from the fovea) and the second axis specifies the rotational
 251 angle of the retinal location; we therefore use the convention of referring to the eccentricity axis on the
 252 colliculus as r and the rotation axis as ϕ .

253 The *cortical magnification factor*, $M(r)$, gives the relationship between the radial eccentricity r and the
 254 retinal neural density. As in Cope et al. (2017), we use a first-order approximation of the form for $M(r)$
 255 given in Rovamo and Virsu (1979):

$$M(r) = \frac{M_f}{1 + \frac{r}{E_2}} \quad (12)$$

256 The foveal magnification, M_f , is the magnification of the most central region of the retina and has a value
 257 in the human of about 7.8 mm/ $^\circ$ (Rovamo and Virsu, 1979).

258 In our model, M_f is related to W_{nfs} , the width of the retinotopic neural field, W_{fov} , the width of the
 259 eye's field of view and E_2 , the eccentricity at which the retinal density has halved by:

$$M_f = \frac{W_{nfs}}{E_2 \ln \left(\frac{W_{fov}}{2E_2} + 1 \right)} \quad (13)$$

260 Here, W_{nfs} is 50 (the side length of the 50x50 grid) and W_{fov} is set to 61 $^\circ$, a reduction from the
 261 biophysically accurate 150 $^\circ$ due to the small number of neurons in the retinotopic neural field. E_2 is 2.5
 262 (Cope et al., 2017; Slotnick et al., 2001).

263 The mapping from the retinotopic co-ordinates in the brain to rotational co-ordinates of the stimulus/
 264 response was written down by Schwartz (1977, 1980) for measurements of striate cortex [visual
 265 stimulus to electrophysiological response—Daniel and Whitteridge (1961); Talbot and Marshall (1941)]
 266 and by Ottes et al. (1986) for superior colliculus data [electrophysiological SC stimulus to eye movement
 267 response—Robinson (1972)]. We used the following statement of this mapping to introduce stimuli into
 268 the ‘World’ input population of the brain model:

$$\phi = \frac{W_{nfs}}{2\pi} \arctan \left(\frac{\theta_y^t}{\theta_x^t} \right) \quad (14)$$

269

$$r = M_f E_2 \ln \left(\frac{1}{E_2} \sqrt{\theta_x^t{}^2 + \theta_y^t{}^2} + 1 \right) \quad (15)$$

270 Note that we use r and ϕ as the co-ordinates on the ‘collicular surface’. Schwartz uses r and ϕ as the polar
 271 coordinates of the retinal stimulus; Ottes et al. use r and ϕ as polar coordinates for the eye movement
 272 response; both use u and v as the Cartesian co-ordinates of the neural map. We use θ_x^t and θ_y^t to give Euler
 273 rotations for the retinal target stimulus. Note also that the form of Eqns. 14 & 15 is slightly different from
 274 that given in Ottes et al. (1986) because our θ_x^t and θ_y^t are not the polar co-ordinates used in that work.

275 The mapping encompasses the entire visual field; the value of ϕ is allowed to vary from 0° to 360° along
 276 its axis. Effectively, the two contralateral colliculi found in the biology are incorporated into a single,
 277 square map, avoiding the need to carry out the kind of ‘colliculus gluing’ described in Tabareau et al.
 278 (2007).

279 It is straightforward to show that the reverse mapping is given by:

$$\theta_x = E_2 \left(e^{\frac{r}{M_f E_2}} - 1 \right) \cdot \cos \left(\frac{2\pi\phi}{W_{nfs}} \right) \quad (16)$$

280

$$\theta_y = E_2 \left(e^{\frac{r}{M_f E_2}} - 1 \right) \cdot \sin \left(\frac{2\pi\phi}{W_{nfs}} \right) \quad (17)$$

281 where we have dropped the t superscript on θ_x & θ_y , as these equations transform a collicular location into
 282 rotations of the eye.

283 Fig. 3 shows the result of the mapping for a view of two cross-shaped luminances. One cross illuminates
 284 the fovea, which results in a large comb-shape of activity. The more peripheral cross produces (in FEF) an
 285 indistinct object centred at a larger value of r .

286 2.2.3 Network

287 Briefly, the model consists of input from the World population (see Fig. 2, green population box)
 288 producing activity in an ‘express’ pathway to superior colliculus (purple) and simultaneously in cortex,
 289 represented here by the FEF population (grey boxes in Fig. 2). The express pathway causes short latency
 290 activity in the superficial superior colliculus, which directly innervates the deeper layers of the superior
 291 colliculus (SC_deep). Activity in FEF generates firing in a thalamo-cortico-basal ganglia loop. The output
 292 of the basal ganglia is the substantia nigra pars reticulata (SNr) which tonically inhibits SC_deep. If a
 293 location of activity in FEF is able to dominate selection in the basal ganglia circuit, the corresponding
 294 location in SNr will dis-inhibit and activity will build up in SC_deep encoding the saccade end point.

295 Connections shown in red are one to one connections; dark blue projections indicate a connectivity pattern
 296 which ‘fans out’ with a 2-D Gaussian kernel; lighter blue connections from the subthalamic nucleus (STN)
 297 to SNr and globus pallidus externum (GPe) are diffuse, all-to-all connections and projections coloured
 298 green are one-to-one connections that decay towards the fovea so that foveal activity in FEF does not swamp
 299 the basal ganglia which would prevent peripheral luminances from ever being selected. Note that SC_deep
 300 contains two recurrent connections; one is excitatory, with a Gaussian kernel mapping and the other
 301 implements tecto-tectal inhibition, which increases the inhibition between activity in opposite hemispheres
 302 of the field of view (Gian G. Mascetti and Jorge R. Arriagada, 1981; Olivier et al., 2000) helping to resolve
 303 competition between saccades to the left and right. The tecto-tectal inhibitory connection is *not* present in
 304 the Cope-Chambers-Prescott-Gurney model. In all other respects the model is as described in Cope et al.
 305 (2017). We have not listed the parameters of the network in tabular form here, instead, the reader is referred
 306 to the SpineML declarative specification of the model from the link given in SUPPLEMENTAL DATA.
 307 The easiest way to access this information is by using SpineCreator.

308 2.3 Brainstem model

309 We implemented a saccadic burst generator (SBG) based on the connectivity outlined in Gancarz and
 310 Grossberg (1998). The SBG network for two of the model’s six channels is shown in Fig. 4. Activity
 311 from the output layer of superior colliculus (SC_avg) is fed into each channel, which sums the activity it

312 receives and processes it in populations each of a single neural element representing all the neurons in that
 313 population. Each channel of the SBG functions to create the motor neuron activations that are required to
 314 accelerate the eye in a particular direction, then hold the eye in its new position against the returning force
 315 generated by the elastic properties of the muscles. The required motor neuron activations are therefore a
 316 combination of features: a brief burst of increased activity that accelerates the eye; followed by a period of
 317 activity that is less than the burst firing rate but higher than the tonic rate that exists when the eye is at the
 318 centre. This holds the eye in its new position.

319 The SBG connectivity produces each of the these features separately, then sums them to create the desired
 320 ‘bump and tonic’ activation time series. The input to the first population in the SBG, the long-lead burst
 321 neurons (LLBNs), is conceived as originating from one of the deep layers of the superior colliculus. The
 322 activity of the LLBNs are passed to excitatory burst neurons (EBNs) which, in turn, inhibit the LLBNs via
 323 the activity of the inhibitory burst neurons (IBNs). This feedback loop has a transmission delay, which
 324 allows activity to build up in the EBNs before the inhibition is activated and the activity is then reduced
 325 again. This mechanism generates the ‘bump’.

326 The generation of the ‘tonic’ phase of the required time series is achieved simply by integrating the
 327 bump over time and multiplying by a some small gain factor. This is the function of the tonic neurons
 328 (TNs). The firing rate of the motor neuron defines the amount of force applied to the eye by that muscle.
 329 Thus, the size of the ‘bump’ defines how far the eye moves in that channel’s direction. The gain and delay
 330 parameters in the LLBN-EBN-IBN-LLBN feedback loop therefore have to be tuned such that the endpoint
 331 of the saccade is reasonably accurate. Furthermore the restoring force generated by the elasticity of the
 332 muscles is dependent on the radial distance. The value of the new tonic firing rate, after the ‘bump’ is
 333 dependent on the end location of the eye. If the ratio between the EBN firing rate and the TN firing rate is
 334 not exactly correct, the eye will drift away from the saccade endpoint after the saccade has been completed.
 335 The EBN-TN connection strength is therefore tuned such that the TN firing rate yields a stable eye position
 336 across a range of eye eccentricities.

337 The omnipause neurons (OPNs) are tonically active and inhibit the EBNs. The activity of the OPNs is
 338 itself inhibited by activity in the LLBNs. The purpose of this arrangement is to ensure the eye does not
 339 move in response to neural noise.

340 Each mean activity of all the neurons in each SBG population (except the TNs) is defined by a single
 341 leaky integrator, first order differential equation.

$$\frac{da}{dt} = \frac{1}{\tau}(y - a) \quad (18)$$

342 where a is the activation of the nucleus, and τ is the time constant of the nucleus. y is a piecewise linear
 343 function of the weighted sum of inputs to the nucleus and is given by

$$y(IN) = \begin{cases} 0 & IN \leq b \\ IN - b & b \leq IN \leq 1 + b \\ 1 & IN \geq 1 + b \end{cases} \quad (19)$$

344 where b is the IN axis offset. IN is the weighted sum of inputs to the nucleus and is given by,

$$IN = \sum_m^M w_{mn} a_m \quad (20)$$

345 where a_m is the activation of the m^{th} afferent nucleus. w_{mn} is the connection strength between the m^{th}
 346 afferent nucleus and the current nucleus. The activity of the TNs are defined as

$$\frac{da}{dt} = \frac{1}{\tau} y \quad (21)$$

347 with an identical piecewise linear transfer function as the other SBG populations.

348 2.4 biomechanical eye

349 The output signals of the brainstem are used to drive the biomechanical model. The latter is not only
 350 used to get tangible feedback on the simulated saccades including motion trajectories, but adds one more
 351 modelling dimension related to the inertial properties of the eye plant including muscle properties.

352 The biomechanical eye model, implemented using the OpenSim framework (Seth et al., 2011), is
 353 anatomically represented by a sphere of uniform mass distribution. The diameter of the eye is 24 mm for
 354 adults, with small variations between individuals; the mass of the eye is 7.5 grams. The eyeball is actuated
 355 by six extraocular muscles (EOMs). The EOMs are arranged in three pairs forming a cone inside the orbit
 356 with the apex being located inside the cranium in a tendonous ring called the annulus of Zinn. An important
 357 feature of the oculomotor system which greatly affects its overall behavior is the existence of dynamic
 358 EOM pulleys. Their role is to guide the pivot point of the EOMs. In our model, a pulley for each EOM has
 359 been modeled by a point on the orbit whose location depends on the current eye orientation.

360 The force applied by EOMs is controlled by an excitatory signal supplied by motoneurons in the brainstem.
 361 The neural drive to produce a saccadic eye movement can be characterized by a pulse component to
 362 overcome the viscoelasticity of the orbital plant, a step component to stabilize the eye in the new position,
 363 and a slide component that models the gradual transition between the pulse and step.

364 The dynamics of muscular forces can be split into: 1) The elasticity of the muscles. 2) A delay between
 365 the onset of the afferent excitatory signal and the actual muscle contraction, caused by the transmission
 366 time of the action potentials and by the necessary calcium release at the muscle fibres. We developed a
 367 custom extraocular muscle model which captures these features.

368 Passive forces due to the fatty tissues inside the eye orbit also affect eye dynamics. Their role is critical in
 369 eliminating the influence of head and body movements. We incorporated a custom torque, t , which acts
 370 like a rotational spring-damper apparatus, resisting eyeball movements. It has elastic and viscous properties
 371 governed by $t = -K\mathbf{R} - C\dot{\mathbf{U}}$ where \mathbf{R} is the eye's orientation and $\dot{\mathbf{U}}$ is its angular velocity. K and C are
 372 constants. A fuller description of the biomechanical model can be found in Papapavlou and Moustakas
 373 (2014).

374 2.5 Integrating the models and closing the loop

375 The Cope-Chambers-Prescott-Gurney model closed its loop by passing the centroid of activity in SC_deep
 376 (once it had surpassed a threshold) back to the code that controlled the world, which would then use this
 377 location to instantaneously change the model's view of the world. In our extended model, it was necessary
 378 to connect the output of the brain model back to its input via the saccadic burst generator model and the
 379 biomechanical eye. The resulting state of the eye, rather than the centroid of the superior colliculus, was
 380 used to compute the input to the brain, given the luminances visible in the world.

381 A number of studies have considered the form of the connection between the deeper layers of the superior
 382 colliculus and the saccadic burst generator (Van Gisbergen et al., 1985; Ottes et al., 1986; Waitzman et al.,

383 1991; Groh, 2001; Arai et al., 1994; Goossens, 2006; Tabareau et al., 2007; Van Opstal and Goossens,
 384 2008; Goossens and Van Opstal, 2012), which has become known as the spatial temporal transform (STT).
 385 The spatial aspect of the transform is thought to be implemented by a weight-mapping (Tabareau et al.,
 386 2007; Arai et al., 1994) and we follow this idea. Arai and co-workers trained a 20x20 neural network model
 387 of the superior colliculus to discover the weight map under the assumption of 2D Gaussian activation
 388 profiles (Arai et al., 1994). The training approach of Arai et al. (1994) was not feasible in this study
 389 due to the length of time required to run our model and its stochasticity, which meant multiple runs
 390 of the model were necessary in order to generate output statistics. Tabareau et al. (2007) wrote down
 391 a theoretical form of the weight map, which follows from the mapping of Ottes et al. (1986) and the
 392 assumption of invariant 2D Gaussian activity profiles in SC. As they found it closely resembles the results
 393 of Arai et al. (1994), and it is a simple formulation, we considered it as the means to generate the six
 394 weight maps in our own model. One barrier to the use of the weight map in Tabareau et al. (2007) was the
 395 Cope-Chambers-Prescott-Gurney model's violation of the *invariant integral hypothesis*. This states that
 396 the number of spikes emitted by a neural element during a saccade (or in our model, the integral of the
 397 neuron's output during the saccade) should be a function only of its position within the hill of collicular
 398 activity. That is, for any time-dependent hill of activity $\mathcal{A}(\mathbf{z}, t)$ at $\mathbf{z} = (r, \phi)$ on the collicular surface, the
 399 integrated activity $A_{\mathbf{x}}$ in an element at a vector \mathbf{x} away from \mathbf{z} is

$$A_{\mathbf{x}} = \int_t \mathcal{A}(\mathbf{z} - \mathbf{x}, t) dt \quad (22)$$

400 which is invariant for all \mathbf{z} . However, the very mapping on which the Tabareau et al. (2007) result is based
 401 leads to a very *variant* activity profile in the Cope-Chambers-Prescott-Gurney model. A luminance of a
 402 given size which excites activity near to the fovea causes activity in a large number of neurons, whereas
 403 activity far from the fovea excites a much smaller region. This effect is clearly demonstrated in Fig. 3 for
 404 equal sized targets both on and distal from the fovea.

405 This led us to hypothesize that the retinotopic mapping be accompanied by an associated widening
 406 projection field such that the hill of activity in superior colliculus is invariant with position on the collicular
 407 surface. There are a number of locations in the system in which this widening projection field could exist.
 408 It could be implemented in the projections between the retinal populations and the superficial layer of
 409 SC along with the projection between the World and the FEF population. However, this would affect
 410 activity within the basal ganglia of the model, contradicting a result in Cope et al. (2017) which explains
 411 the 'hockey stick' profile for saccade latency as a function of saccade eccentricity. Instead, we suggest
 412 that a widening projection field is encoded within the superior colliculus itself, a complex, multi-layered
 413 structure which could quite plausibly support such a function. Indeed, such widening activity can be seen in
 414 the stimulation experiments in Vokoun et al. (2010) and Vokoun et al. (2014). Although in this work we do
 415 not model the SC in detail, we extended the model with a third functional layer named SC_deep2, shown in
 416 Fig. 5 (Cope-Chambers-Prescott-Gurney has only the two layers SC_sup and SC_deep). We introduced a
 417 widening projection based on a Gaussian projection field whose width, $\sigma(r)$ varies in inverse proportion to
 418 the magnification factor, $M(r)$, given in Eq. 12 according to:

$$\sigma(r) = \frac{m_\sigma}{M(r)} - \frac{m_\sigma}{M^0} + \sigma_0 \quad r > r_0 \quad (23)$$

419 m_σ is a scalar parameter which determines the 'magnitude of the widening'. M^0 is the 'starting' magni-
 420 fication factor; within the foveal region ($0 \leq r \leq r_0$), the projection field is not allowed to widen and

421 so

$$\sigma(r) = \sigma_0 \quad r \leq r_0 \quad (24)$$

422 which makes σ_0 the width of the Gaussian projection field within the foveal region. (Note that the value
 423 chosen for the width of the foveal region, r_0 is not identical to the foveal shift parameter used in the
 424 *DecayingAtFovea* projections into striatum.) The *Widening Gaussian* projection weight, $w(r, d)$ is then
 425 computed as:

$$w(r, d) = e^{-\frac{d^2}{2\sigma(r)^2}} \quad (25)$$

426 where d is the distance between the source and destination elements in the collicular plane. m_σ was set to
 427 50, σ_0 was 0.3, M^0 was 12.43 and r_0 was 20.

428 A further issue regarding the use of the theoretical weight map in Tabareau et al. (2007) was that it does
 429 not consider the existence of the oblique extraocular muscles. There is evidence that only two dimensional
 430 information is encoded in superior colliculus (Wurtz and Goldberg, 1972; Hepp et al., 1993; Van Opstal
 431 et al., 1991), but the eye is actuated by six extraocular muscles. In order to find out a possible form for the
 432 input to the oblique muscles we carried out a training process which depended on a centroid computation
 433 in SC_deep. For the four rectus muscles, the resulting weight maps resembled those found by Arai et al.
 434 (1994). The trained maps for the oblique muscles had a form very close to those for the inferior and
 435 superior rectus channels, but with a smaller magnitude. The inferior oblique map resembled the superior
 436 rectus map and the superior oblique map resembled the inferior rectus. When parameterising the theoretical
 437 weight maps, we set the inferior/superior oblique maps to be 1/10th of the superior/inferior rectus maps,
 438 respectively. Interestingly, this suggests that there is a built-in synergy between the vertical and oblique
 439 channels in the eye, although the results will show there is some systematic change in the oblique error
 440 with saccade end-point location.

441 Tabareau et al. (2007) gives a formulation for the weight maps in which it is possible to project both a
 442 positive and a negative weight. In our model, all projections from SC_deep are excitatory. This means that
 443 each channel has a weight which follows the form:

$$w(r, \phi) = i e^{jr} \sin \left(\frac{2\pi\phi}{W_{nfs}} + k \right) \quad (26)$$

444 where i , j and k are per-channel parameters for the weight maps. k is determined by the mapping. Only the
 445 positive part of the sine is utilised. i and j are parameters to be found.

446 The saccadic burst generator model was originally conceived with the assumption of a step input, which
 447 returns to zero activity at a suitable time to curtail the saccade and avoid staircase saccades (Gancarz and
 448 Grossberg, 1998). In our model there is no such mechanism to reduce activity in SC_deep, and elsewhere.
 449 Although a successful, accurate saccade towards a target luminance will remove the excitation which caused
 450 the activity in SC_deep by bringing the target luminance within the masked, foveal region, the activity
 451 in SC decays too slowly to avoid additional saccadic movements. We found it necessary to hypothesize
 452 an inhibitory feedback mechanism from the SBG to the brain model. This is shown in Fig. 4, which
 453 indicates how the output from the inhibitory burst neurons (IBN) of the SBG model are used to feed back
 454 an inhibitory signal to the SC_deep, thalamus and FEF populations in the brain model, resetting them ready
 455 for the next saccade.

456 The output signals from the six channels of the SBG were connected to the six motoneuron inputs of the
 457 biomechanical eye. The signal was normalised; a value of 1 meaning that all the motoneurons in the output

458 population were firing at their maximum rate and the force exerted by the relevant extraocular muscle
459 was maximal. Channels innervated extraocular muscles as follows: Up: superior rectus; Down: inferior
460 rectus; Right: medial rectus; Left: lateral rectus; Z+: superior oblique; Z-: inferior oblique. Because the
461 medial rectus induces a rightward rotation of the eye, our single virtual eye is a *left* eye. The OpenSim
462 implementation of the biomechanical eye was ‘wrapped’ (in the software sense) in a BRAHMS component.
463 This made it possible to integrate the OpenSim model into the BRAHMS framework. The wrapper ensured
464 that the input and output signals were correctly transferred and, importantly, handled the disparity in the
465 solver timesteps used in the OpenSim model (25 ms) and the neural model (1 ms). This was achieved by
466 having the BRAHMS wrapper create a separate thread to run the OpenSim model. The BRAHMS wrapper
467 component was called on each 1 ms timestep, receiving the instantaneous activations from the motoneurons
468 in the SBG. These activations, and the current simulation time, were written into a shared memory area,
469 accessible by the OpenSim thread. Running independently, the OpenSim thread would update its inputs
470 (using the most recent values in the shared memory area) whenever the simulation time had increased
471 by 25 ms. It would then recompute its outputs (the rotational state of the eye) and write these into the
472 same shared memory. The BRAHMS wrapper would update its outputs whenever they were changed in
473 the shared memory by the OpenSim thread. A direct connection of the six outputs of the BRAHMS eye
474 model component to the six inputs of the worldDataMaker BRAHMS component was specified in the
475 SpineML_2_BRAHMS external.xsl file.

476 The eye model outputs its rotational state at each timestep. The rotational state is used to compute
477 the view of the world in the eye’s frame of reference. To simplify the calculation, the luminances exist
478 on a spherical surface at the centre of which is the eye. A hand-coded BRAHMS component called
479 worldDataMaker computes the projection of the luminances into the eye’s frame of reference and then
480 converts this representation into a retinotopic map to pass into the brain model. The input to the brain
481 model is thus able to change continuously, on every timestep, rather than in a step-wise fashion when a
482 saccade occurs, as in the Cope-Chambers-Prescott-Gurney model.

483 In the worldDataMaker BRAHMS component, the rotational state of the eye was used to construct
484 Euler rotation matrices which transformed between the world’s frame of reference and the eye’s frame of
485 reference. The worldDataMaker component received a specification of the world luminances in a JSON
486 file called luminances.json at the start of each simulation. luminances.json specified the position, shape,
487 size, luminance, appearance time and disappearance time of an arbitrary number of luminances. With this
488 information, the instantaneous rotational state of the eye and the parameters of the retinotopic transform, it
489 was able to compute the instantaneous input to the brain model.

490 The final models, on which the results of this paper are based are named ‘TModel3’, ‘TModel4’ and
491 ‘TModel5’. Descriptions of these, and earlier versions of the model can be found in the code repository
492 given in SUPPLEMENTAL DATA.

3 RESULTS

493 3.1 Weight maps

494 We found the best parameters for the exponential in Eq. 26 (i and j) by a manual tuning process. After
495 selecting values for i and j in either the horizontal or vertical/oblique channels, we ran the model 6 times
496 at each of 8 target eccentricities (7° – 14°) which were purely in the direction of the newly parameterised
497 channel. The training saccades were produced as described below in Sect. 3.3, with the same fixation
498 and target luminances (crosses of magnitude 0.2 and 0.3) but with the fixation offset and target onset

499 occurring at 0.2 s. We measured the end-point of the saccade by detecting the location at which the saccade
500 velocity had dropped below 0.005 of its peak. We iterated until the mean saccade endpoint plotted versus
501 target was close to the ideal straight line—see Fig. 6(a) & (c). We applied the same parameters to both
502 directions of each channel; $i_{up} = i_{down} = 0.00195$, $j_{up} = j_{down} = 0.075$, $i_{left} = i_{right} = 0.0016$ and
503 $j_{left} = j_{right} = 0.067$. The resulting weight maps (where the oblique maps are 1/10th of the vertical maps,
504 as described earlier) are shown in Fig. 7.

505 3.2 Saccade accuracy

506 In Fig. 6, we showed the result of running the model to targets located on the principle axes, on which
507 the model was trained. We then simulated single saccades to targets in one hemifield of the eye's field of
508 view, with eccentricities between 6° and 14.5°. As in the training, we ran the simulation 6 times for each
509 target, $\theta^t = (\theta_x^t, \theta_y^t, 0)$ to obtain mean saccade end-points. Fig. 8 shows saccade accuracy results for an
510 entire hemifield in the naïve model which passed the output of SC_deep directly to SBG via the weight
511 maps. The ratio of the magnitude of the error vector to the magnitude of the target vector is plotted using
512 a colour map. This ratio is shown for the full, three dimensional error vector in Fig. 8(a) and for the x ,
513 y and z components in Figs. 8(b)–(c). Inspection of Fig. 8(a) shows that the end-point error is minimal
514 along the principle axes ($\theta_x^t = 0$ or $\theta_y^t = 0$) and maximal near the 45° oblique targets (blue lines) with the
515 end point error as high as 80% of the programmed saccade magnitude. The x component error map in
516 Fig. 8(b) shows the same trend, mirrored about the 'Target X' axis, whereas the y and z component errors
517 are, relatively, much smaller. Because the x component of the error is clearly contributing to end point
518 errors which would not be considered 'on target', especially for oblique saccades, we considered the effect
519 of the non-uniform size of the hill of activity in SC_deep.

520 In our model, the location, *size* and shape of activity in FEF, the basal ganglia, thalamus and superior
521 colliculus is eccentricity dependent, in line with the retinotopic mapping stated by Ottes et al. (1986). More
522 eccentric targets generate reduced activity, because fewer retinal neurons are excited far from the fovea.
523 Cope et al. (2017) showed that this relationship can explain increased saccadic latencies for distal targets,
524 resulting from reduced activity in the decision making circuitry of the basal ganglia. However, the notion
525 that activity in superior colliculus is eccentricity-dependent conflicts with the result of Tabareau et al. (2007),
526 who showed that an invariant hill of activity was required if this complex logarithmic weight mapping was
527 to be used to drive a two-degree-of-freedom saccadic burst generator, and also with experimental findings,
528 which do not show significant eccentricity dependence, at least in the burst layer (Anderson et al., 1998).

529 To bring our model in line with these results, whilst maintaining the eccentricity dependent activity in
530 basal ganglia, we hypothesised that a 'widening projection' exists between two maps in superior colliculus.
531 Activities in one SC_deep layer remains eccentricity-dependent, with loops back to thalamus and cortex and
532 through basal ganglia. This activity is then fed through a projection, which applies a Gaussian projection
533 field, whose width increases with increasing stimulus eccentricity according to Eq. 25. The activity in
534 this second SC_deep layer is then fed to the weight maps of the SBG. This model was called 'TModel4'.
535 TModel4 was parameterised such that its horizontal and vertical error was similar—so that its equivalent of
536 Fig. 6 showed a similar sum of squares error.

537 Figs. 9(a)–(d) show the same percentage errors for TModel4 as Fig. 8 shows for TModel3. First of all,
538 note that the error magnitudes are much smaller. The mean errors are smaller for every axis. The largest
539 errors produced by the model are approximately 15%, which are within the boundaries of what some
540 authors have suggested would be regarded as an accurate saccade (McPeek and Keller, 2002; McPeek,
541 2006). The magnitude of the largest error vector is approximately 1.5°.

542 This result indicates that the exponential part of the Ottes et al. weight map from SC to the SBG cannot on
543 its own compensate for the eccentricity-dependent size of the hill of activity. The introduction of a widening
544 projection field substantially improves the mean accuracy of saccades across the field of view. We therefore
545 suggest that the transformation between retinotopically mapped activity, and eccentricity-independent
546 activity width occurs within the superior colliculus and works alongside a simple, monotonically increasing
547 weight map between SC and the SBG channels.

548 3.3 Single saccades

549 Having finalised the model by setting the weight maps, we then proceeded to exercise the model
550 (TModel4), starting with saccades to a single target; prosaccades. Fig. 10(a) shows 9 representative
551 saccades to a single target luminance. Initially, the eye had rotational state $\theta_x = \theta_y = \theta_z = 0$ with
552 its fovea directed at a fixation luminance cross (span 6°, bar width 2°) of magnitude 0.2 (in arbitrary
553 units). At a simulation time of 0.4 s, the fixation luminance was set to 0 and a target luminance cross
554 of the same dimensions as the fixation but with magnitude 0.3 was illuminated at one of the 9 different
555 locations, marked by crosses in Fig. 10(a). The resulting trajectories are plotted, with colour indicating the
556 relationship between trajectories and target crosses. The approximate end-point error is visible in this figure,
557 although the last point in each trajectory is the saccade position at 0.8 s and not the velocity-based end-point
558 described above. Figs. 10(b) and (c) show the rotational components of the blue and red trajectories in
559 Fig. 10(a) along with the target and fixation luminance values. Rotations are the eye's Euler rotational
560 components in the world frame of reference.

561 3.4 Saccade Latencies

562 To verify that our implementation of the brain model has the same functionality as that reported in Cope
563 et al. (2017), we investigated the effect on saccadic response times of: target eccentricity; and any gap
564 or overlap between fixation off-time and target on-time. We showed that the full model reproduces the
565 'hockey stick' shape shown in Fig. 7 of Cope et al. (2017) for horizontal [Fig. 11(a)], vertical [Fig. 11(b)]
566 and oblique saccades (not shown). The latency increases with eccentricity far from the fovea because
567 the retinotopic mapping reduces the activity in the basal ganglia for more eccentric targets (this effect is
568 described in detail in Cope et al. (2017)). Closer to the fovea, the interaction between the foveal mask and
569 the activity in FEF again leads to reduced input into the basal ganglia and an increased time to achieve
570 disinhibition in SNr.

571 Fig. 11(c) shows latencies achieved when varying the time between fixation offset and target onset. This
572 is termed the *gap condition*; and is represented by a scalar value which, if positive, refers to a gap between
573 fixation offset and target onset, and when negative, signifies an overlap, with the fixation luminance
574 persisting past the time at which the target is illuminated. A negative gap is also termed an *overlap*. Again,
575 we verify the behaviour presented in Cope et al. (2017), explained as resulting from the inhibition of
576 the cortico-thalamic loop by SNr. In the gap condition, when the fixation luminance is removed, activity
577 in STN immediately begins to decay, allowing SNr activity to reduce and thereby reducing inhibition
578 on thalamus, allowing the target luminance to build up quickly in FEF, thalamus and through the basal
579 ganglia's striatum and SNr. The shape of the curves in Fig. 11(c) matches the results in Cope et al. (2017)
580 for target luminances of 1 and 0.6; for overlaps longer than 100 ms (gap < -100 ms), the latency becomes
581 constant; the saccade is programmed whilst the fixation is present, with the target luminance inducing
582 sufficient activity in striatum to 'break through' the SNr inhibition caused by the fixation. If the target
583 luminance is reduced to 0.3, the balance is altered in favour of the fixation and the latency vs. gap becomes
584 approximately linear and equal to the overlap time plus around 100 ms.

585 Fig. 11(d) shows the effect of the dopamine parameter on saccade latencies in gap, step and overlap
586 conditions. In general, the effect of decreasing the dopamine parameter was a smooth, monotonic and
587 undramatic increase in saccade latency. However, the data for the overlap condition with a target luminance
588 which was 3 times as bright as the fixation luminance was more interesting. Here we see a transition around
589 a dopamine value of 0.7. Below this value, the basal ganglia is not able to select the target luminance until
590 the fixation is removed, reducing the excitatory drive from STN to SNr, and consequently the inhibition
591 from SNr to the thalamo-cortical loop. For the target luminance 0.6, 0.7 dopamine allows the basal ganglia
592 to select sufficiently well so that the target can build up in the thalamo-cortical loop, in spite of the fixation
593 overlap.

594 The relationship between latency and the target luminance is given in Fig. 11(e). This shows latency for a
595 100 ms gap, step and 100 ms overlap conditions for a given fixation luminance of 0.2, and a horizontally
596 located target at $\theta_y^t = -10^\circ$. For the gap condition, we see very short latencies for luminances of about
597 0.75 and above. Finally, the activity driving these express saccades is initiated by high firing rates in the
598 superficial layer of SC (SCs), which then drives activity in thalamus and through the basal ganglia. A
599 gradual transition from express saccades to reflexive saccades is observed as the contribution of the SCs
600 becomes weaker and the drive from FEF into the thalamo-cortical loop becomes necessary to elicit a
601 saccade. A similar gradual transition, albeit for higher latencies is seen for the step condition. At higher
602 target luminances, the SCs has a greater effect on the activity in the thalamo-cortical loop. However, the
603 activity in STN caused by the fixation luminance increases the latency at all luminance values compared
604 with the gap condition. The overlap condition leads to increased latencies for luminances below 2.5, but
605 meets the step condition above this value, at which the 0.2 fixation luminance appears to have a negligible
606 effect on the system.

607 3.5 Saccade sequences

608 We now present results derived from the fully parameterised and integrated model; where we took
609 advantage of the fact that it is a closed loop system. This allowed us to present sequences of target
610 luminances and allow the model to direct its fovea at the most salient target.

611 3.5.1 Out & return

612 We investigated the behaviour of the model for saccade sequences. In one experiment, we illuminated
613 a fixation cross from 0 s until 0.4 s, followed by a target at $(0, -10^\circ)$ from 0.4 s until 0.8 s. Finally, the
614 fixation was again shown from 0.8 s until the end of the simulation at 2 s. This induced a saccade to a
615 10° eccentricity, followed by a return saccade back to the null point. We noticed some irregularities in the
616 return saccades, which though surprisingly accurate, had a significant overshoot. More perplexingly, if the
617 target was switched repeatedly between 0° and 10° , second and subsequent *outward* saccades also showed
618 this overshoot. We found that the cause of these irregularities was the lack (in ‘TModel4’) of any mechanism
619 to reset the tonic neurons in the SBG after the first saccade. This resulted in TN activity in the left channel
620 *and also* in the right channel. Interestingly, this ensured that, at least for a few, consecutive out-and-return
621 saccades, the saccade accuracy was relatively good, with trajectories resembling experimental data (Bahill
622 and Stark (1979), p. 6). Nevertheless, the lack of a reset of TN activity was an oversight, and is indeed
623 proposed and included in the connectivity of the Gancarz and Grossberg (1998) model. We implemented
624 this feature by adding an additional inhibitory input to the ‘integrator’ component of TModel4, driven
625 by the contralateral EBN population, naming the new model ‘TModel5’. Now, when the eye is directed
626 towards an eccentric target which is then exchanged with a target at the null point, the EBN activity toward

627 the null point will tend to extinguish the TN activity which was holding the eye at the eccentric position.
628 We verified that none of the single saccade results were affected by this modification.

629 Fig. 12 shows the outward and return trajectories produced by the experiment with the TN reset mecha-
630 nism. Panel (a) shows the x and y rotation trajectory; panel (b) shows individual rotational components of
631 the eye. Fig. 12(c) shows out and return trajectories for three other saccade targets; horizontal, vertical and
632 oblique. The trajectories have characteristic shapes and also show some stochastic variation caused by the
633 noise in the model [see dashed trajectories in Fig. 12(a)].

634 The return trajectories (magenta lines) showed a distinctly different form from the outward trajectories.
635 They overshot their destination (the null point) significantly. This resulted from the removal of the TN
636 activity which was holding the eye at the eccentric target location. Removal of this activity, and thus the
637 static force exerted by the corresponding extraocular muscle, meant that the eye was subject both to a new
638 muscular force towards the null point *alongside* the restorative spring force of the lengthened rectus muscle.
639 This stands as a shortcoming of the model.

640 3.5.2 Double steps

641 In another experiment, we probed the response of the model to double step stimuli of the type described
642 in Becker and Jürgens (1979). In that work, the response of human subjects was investigated when shown
643 stimuli at 15° and 30° eccentricity with variable delay between the stimuli. If the smaller eccentricity
644 stimulus was shown first, followed by the more distal on the same side of the field of view, this was called
645 a ‘staircase’ presentation. We carried out a ‘staircase’ presentation, shown in Fig. 13, where our small
646 eccentricity luminance was at 8° and our more distal luminance was at 12° (both to the right of centre). We
647 found that there was a critical time delay between the luminances of about 30 ms. If they were presented
648 with a delay smaller than this value, then a single, slightly hypermetric saccade was made. This response
649 type is called a *final angle response*. A delay greater than 30 ms between the stimuli would lead to double
650 step saccades (a so-called *initial angle response*), with the first saccade arriving at 8° (though with greater
651 variability than normal), and a second saccade being made to a location hypometric of 12° after a pause
652 of about 240 ms. Fig. 13(a) shows the mean trajectories from 5 simulations of the staircase doublestep
653 presentation alongside the result for a single saccade to the final angle of 12° . Dash-dot lines show ± 1
654 standard deviation about the mean. The corresponding trajectories are shown in Fig. 13(b).

655 Inspection of the activity maps in FEF and SC_deep (not shown) indicates that when the 8° target
656 is illuminated for 30 ms or more, the activity associated with this target angle is able to dominate the
657 activity, hence the execution of a reasonably accurate saccade. The inhibitory feedback from the SBG then
658 extinguishes activity in FEF, thalamus and SC, which means that a full 200 ms or more is required to allow
659 activity in these populations to build up again in order to make the smaller saccade from 8° to 12° . This is
660 in contrast to experimental findings in which the corrective second saccade is often executed *more quickly*
661 than if it were programmed on its own (Becker and Jürgens, 1979).

4 DISCUSSION

662 The aim of this study was to demonstrate the importance of modelling neurological systems *in concert with*
663 the biomechanical systems with which they have evolved in parallel. We hypothesised that by combining
664 existing neurophysiological models with an accurate model of a musculo-skeletal system, and then ‘closing
665 the loop’ by allowing the movements of the virtual muscles to modulate sensory feedback to the brain model,
666 shortcomings in the constituent models would be revealed, leading to new knowledge. To demonstrate the

667 validity of this hypothesis, we built an integrated model and then identified the modifications which were
668 necessary to give it the ability to make accurate movements under one type of stimulus. We then examined
669 its behaviour with other stimuli.

670 We chose the oculomotor model as a basis for this study because it has only three degrees of freedom,
671 making it one of the simplest musculo-skeletal systems. Furthermore, eye movements fall into several
672 well-defined categories, each being controlled by separate brain circuits, we were therefore justified in
673 modelling a system which produced only saccadic eye movements. Nevertheless, we are aware that we
674 did not create a complete model of the system; no treatment of the cerebellum was attempted, justified
675 because cerebellum appears to have only a minor effect on saccade accuracy (Dean and Porrill, 2008),
676 probably correcting for slow to medium timescale changes in the physical dynamics of the eyeball (Dean
677 et al., 1994).

678 To summarise our model integration: We combined the Cope-Chambers-Prescott-Gurney model (Cope
679 et al., 2017) with a saccadic burst generator model based on the work of Gancarz and Grossberg (1998),
680 using this to drive the input of a new biomechanical eye model. To achieve the spatial transformation from
681 the retinotopic maps of the Cope-Chambers-Prescott-Gurney model to the six ‘muscle channel’ inputs
682 for the saccadic burst generator, we used the mapping of Ottes et al. (1986) to produce parameterised
683 weight maps along with an empirically discovered synergy for the torsional weight maps. We introduced an
684 additional transformation to the brain model to achieve invariant sized hills of activity in superior colliculus
685 to fulfil the invariant integral hypothesis of Tabareau et al. (2007). We closed the loop using a software
686 component which transformed a view of a world containing luminous cross shapes into the eye’s frame
687 of reference, given its instantaneous rotational state. This component also computed the inverse of the
688 mapping from Ottes et al. (1986) to project the view retinotopically into the brain model. This paper
689 serves to describe how we achieved the integration in order to test our hypothesis, and we intend that the
690 material and methods section, along with the model code itself, will help others to carry out similar studies.
691 However, we wish to devote the majority of this discussion to what can be learned from an integrated
692 model of a combined brain and biomechanical system, using our oculomotor system as an example.

693 Our integration approach revealed three ways in which this model fails to provide a full understanding
694 of the saccadic system. In each case, the issue is made clear *as a result of the integration*. This is not to
695 say that other approaches may not also reveal shortcomings; we will see that one of our cases has been
696 independently identified (Groh, 2011).

697 4.1 The need for a widening projection field

698 The original combination of the Cope-Chambers-Prescott-Gurney model with the theoretical weight maps
699 of Ottes et al. (1986) and Tabareau et al. (2007) resulted in a model which was able to produce accurate
700 saccades only along the principle rotational axes (Fig. 8). Thus, *the integration of the models* suggested
701 that an additional layer was required to achieve accurate saccades for oblique, as well as for horizontal
702 and vertical saccades. Although the *need* for an invariant integral is discussed in Tabareau et al. (2007) as
703 resulting from their theoretical study, the mechanism by which such an invariant Gaussian hill is generated
704 is not. By combining the models, we were forced to consider this mechanism, and hypothesised that a
705 widening projection field would be a candidate mechanism. The results of Fig. 9 indicate that a substantial
706 improvement in accuracy is indeed achieved by this new mechanism.

707 **4.2 Saccades from non-null starting positions**

708 The implementation of a biophysically accurate model of the eye, and the closed-loop nature of the
709 model makes it very natural to consider how the model will behave making saccades from arbitrary starting
710 positions, or how it would respond to a sequence of stimuli. This was the motivation for the out-and-return
711 experiment (Fig. 12) as well as for the double step experiment (Fig. 13). We found that return saccades were
712 substantially affected by the biomechanics of the eye, as the brain and brainstem model had no mechanism
713 to account for the position-dependent restoring forces applied by the eye. This question has been addressed
714 by other authors; Groh (2011) investigates the effect of initial eye position on stimulated saccades and finds
715 a need for the signal in superior colliculus to be modulated by an eye position signal. Ling et al. (2007)
716 shows the existence of a position dependent firing rate offset in abducens neurons. Though we will not
717 speculate here on the mechanism by which return saccades may be made accurate whilst also resetting
718 the activity of tonic neurons in the SBG, it is interesting that in the model in which we omitted to reset
719 TN activity (TModel4), we obtained relatively accurate out-and-return saccades which closely resembled
720 experimental data. We suggest that residual activity in TN populations may offer an explanation for how
721 the restorative force exerted by the elastic oculomotor muscles is compensated for. A comparison of this
722 idea with that of Groh (2011) (that there is a modulation, from a brainstem signal, of the SC readout) would
723 make a subject for a future study. Although these existing studies have highlighted this issue, the inaccurate
724 return saccades which the model makes from eccentric starting positions provide a clear example of the
725 way in which integrating known models into a closed-loop system can highlight deficiencies in the model.

726 **4.3 Inhibitory feedback from saccadic burst generator to brain**

727 The third issue raised by the integration of the component models of the saccadic system has, like
728 the return saccades, to do with resetting activity. In this case, rather than the reset of activity in the TN
729 population in the brainstem, it is the question of how the activity in the *brain* model should be reset after
730 each saccade. When a target luminance is projected onto the World population in the model, this induces
731 activity which ‘reverberates’ in loops through FEF, basal ganglia, SC and thalamus. The brainstem contains
732 a mechanism to limit the timescale of a saccade (inhibitory feedback from EBN, via IBN to LLBN; see
733 Fig. 4). However, if the activity in SC is not reset, then following the completion of the first saccade, a
734 series of subsequent ‘staircase’ saccades will be executed. There needs to be a mechanism to extinguish
735 activity in SC, but also in FEF and thalamus, as activity in either of these populations can build up and
736 eventually cause repeat activity in SC and another saccade. We added hypothetical inhibitory feedback
737 connections to our model, such that the IBN populations in the SBG would inhibit activity in FEF, thalamus
738 and SC_deep (Fig. 4), preventing the occurrence of staircase saccades.

739 An examination of the behaviour of the model when presented with ‘double-step stimuli’ reveals a
740 problem with this scheme. We found that when double-step stimuli were presented (where an initial target
741 at 8° was replaced with a 12° target after 30 or 40 ms) and a double saccade was made [Fig. 13(a), black
742 lines] the second saccade latency was *longer* even than the initial saccade. This contrasts with Becker and
743 Jürgens (1979) who find that second, corrective saccades occur with *shorter* latencies. This suggests that
744 the inhibitory reset signal implemented in this model is too strong or has the wrong timescales. This issue
745 highlights the fact that connections *between* component models are quite as important as the connections
746 within each model.

747 4.4 Concluding remarks

748 The omission of the cerebellum will not have escaped the reader's notice. Whilst many of the nuclei
749 known to be involved in the production of saccadic eye movements are incorporated within the model,
750 the cerebellum is not. The cerebellum is known to play an important rôle in saccade programming (Dean
751 et al., 1994; Schweighofer et al., 1996; Quaia et al., 2000; Kleine, 2003). It may be able to completely
752 replace the functionality of the colliculus when lesioned (Aizawa and Wurtz, 1998; Lefvre et al., 1998).
753 However, this rôle is typically considered to be one of accuracy tuning (Barash et al., 1999; Dean et al.,
754 1994); operating as an additive model. Furthermore, saccades made by individuals with cerebellar ataxias
755 perform with only moderate loss of saccade accuracy (Barash et al., 1999; Federighi et al., 2011). Because
756 we did not address learning in our model, and because our aim was to demonstrate the utility of integrating
757 brain with biomechanics in order to highlight deficiencies, we considered the omission of the cerebellar
758 nuclei acceptable in the present work.

759 We have not addressed the question of saccade duration in this paper. Saccade duration is of interest in
760 models which produce two (or three) dimensional saccades, because the dynamics of a saccade follow well
761 known relationships with the saccade eccentricity, regardless of the saccade angle. This causes a problem for
762 models (such as the present one) for which some of the dynamic behaviour is generated within orthogonal
763 components. For example, saccade duration increases with target eccentricity. A 10° eccentricity oblique
764 (45° up and right) saccade is composed (approximately) of a 7° upwards component and a 7° rightwards
765 component. If the component based model is responsible for the dynamics, then the 10° oblique saccade
766 would be expected to have the dynamics of a 7° up or 7° right saccade. This is not found in practice, and
767 the components are said to have been stretched, hence the name for this effect 'component stretching'. The
768 Gancarz and Grossberg (1998) model is reported to take account of the component stretching effect via
769 the OPN neuron population. We did not find this effect in our implementation of the model; the duration
770 of oblique saccades at a given eccentricity was always substantially different from the duration of the
771 corresponding purely vertical or horizontal saccade. Because there is a somewhat complicated interplay
772 between the dynamics of the superior colliculus driving the dynamic system of the SBG, we feel this is
773 outside the scope of the current work and a subject for a future paper.

774 This work represents a step forward in the modelling of neuromuscular systems, not because it sig-
775 nificantly advances any of the constituent models, but because it *integrates* the models into a complete,
776 *behaving* system. This is not the first integrated brain model composed of separately developed components.
777 The works of N'Guyen et al. (2014) and Thurat et al. (2015) are both based on an example of a brain model
778 which drives a simple, second order model of the eye. DeWolf et al. (2016) describes a reach model which
779 integrates models of cortex and cerebellum to drive a two degree-of-freedom arm model. Both of these
780 example systems nevertheless operate using 'curated' inputs supplied by the modeller.

781 In contrast, the current work allows the state of the system to determine the input delivered to the model.
782 The modeller only curates the state of the world at each time point, but the actual input to the model
783 depends on the eye's rotational state. This is, to our knowledge, the first model which integrates the brain
784 with an accurate biophysical system and closes the loop in this way, enabling the system to reproduce
785 behaviour. As such, it offers a platform for testing more complex saccadic behaviour such as antisaccades
786 or saccades in the presence of distractor stimuli. We believe that by building closed loop systems which
787 express behaviour, we, and others will develop a new field of *computational neurobehaviour*, which will
788 share themes from neuroscience, artificial intelligence, decision science and embodied robotics.

DISCLOSURE/CONFLICT-OF-INTEREST STATEMENT

789 The authors declare that the research was conducted in the absence of any commercial or financial
790 relationships that could be construed as a potential conflict of interest.

AUTHOR CONTRIBUTIONS

791 SJ, AB and AC implemented existing parts of the model in SpineML. AB developed the saccade generator
792 brainstem model. SJ performed the technical and scientific integration of the biomechanical eye. CP and
793 KM developed the biomechanical eye model. SJ wrote the manuscript; SA, AB, KG and KM contributed
794 to the manuscript. KG conceived the project.

ACKNOWLEDGEMENTS

795 *Funding:* European Union FP7 Grant 610391 ‘NoTremor’.

SUPPLEMENTAL DATA

796 The model specification, results and all code required to reproduce the results of this work are available at:
797 https://github.com/ABRG-Models/OMM_NeuroMuscular

REFERENCES

- 798 Aizawa, H. and Wurtz, R. H. (1998). Reversible inactivation of monkey superior colliculus. I. Curvature of
799 saccadic trajectory. *Journal of neurophysiology* 79, 2082–2096
800 Alex Cope and Paul Richmond (2014). SpineML. RRID: SCR_015641
801 Anderson, R. W., Keller, E. L., Gandhi, N. J., and Das, S. (1998). Two-dimensional saccade-related
802 population activity in superior colliculus in monkey. *Journal of Neurophysiology* 80, 798–817
803 Arai, K., Keller, E., and Edelman, J. (1994). Two-dimensional neural network model of the primate
804 saccadic system. *Neural Networks* 7, 1115. doi:10.1016/S0893-6080(05)80162-5
805 Bahill, A. T. and Stark, L. (1979). The trajectories of saccadic eye movements. *Scientific American* 240,
806 108–117
807 Barash, S., Melikyan, A., Sivakov, A., Zhang, M., Glickstein, M., and Thier, P. (1999). Saccadic dysmetria
808 and adaptation after lesions of the cerebellar cortex. *Journal of Neuroscience* 19, 10931–10939
809 Becker, W. and Jürgens, R. (1979). An analysis of the saccadic system by means of double step stimuli.
810 *Vision Research* 19, 967–983. doi:10.1016/0042-6989(79)90222-0
811 Bevan, M. D. and Wilson, C. J. (1999). Mechanisms underlying spontaneous oscillation and rhythmic
812 firing in rat subthalamic neurons. *The Journal of neuroscience : the official journal of the Society for
813 Neuroscience* 19, 7617–28
814 Blenkinsop, A., Anderson, S., and Gurney, K. (2017). Frequency and function in the basal ganglia: the
815 origins of beta and gamma band activity. *The Journal of Physiology* doi:10.1113/JP273760
816 Bogacz, R. and Gurney, K. (2007). The basal ganglia and cortex implement optimal decision making
817 between alternative actions. *Neural Computation* 19, 442–477. doi:10.1162/neco.2007.19.2.442
818 Brown, P., Oliviero, A., Mazzone, P., Insola, A., Tonali, P., and Di Lazzaro, V. (2001). Dopamine
819 Dependency of Oscillations between Subthalamic Nucleus and Pallidum in Parkinson’s Disease. *J.
820 Neurosci.* 21, 1033–1038

- 821 Casteau, S. and Vitu, F. (2012). On the effect of remote and proximal distractors on saccadic behavior: A
822 challenge to neural-field models. *Journal of vision* 12, 14
- 823 Cope, A., Chambers, J. M., Prescott, T. J., and Gurney, K. N. (2017). Basal Ganglia Control Of
824 Reflexive Saccades: A Computational Model Integrating Physiology Anatomy And Behaviour. *bioRxiv*
825 doi:10.1101/135251
- 826 Cope, A. J. and James, S. S. (2015). SpineML_2_BRAHMS. RRID: SCR_015640
- 827 Cope, A. J., Richmond, P., and Allerton, D. (2014). The SpineML toolchain: enabling computational neu-
828 roscience through flexible tools for creating, sharing, and simulating neural models. *BMC Neuroscience*
829 15, P224
- 830 Cope, A. J., Richmond, P., and James, S. S. (2015). SpineCreator. RRID: SCR_015637
- 831 Cope, A. J., Richmond, P., James, S. S., Gurney, K., and Allerton, D. J. (2016). SpineCreator: a
832 Graphical User Interface for the Creation of Layered Neural Models. *Neuroinformatics* doi:10.1007/
833 s12021-016-9311-z
- 834 Daniel, P. M. and Whitteridge, D. (1961). The representation of the visual field on the cerebral cortex in
835 monkeys. *The Journal of Physiology* 159, 203–221. doi:10.1113/jphysiol.1961.sp006803
- 836 Dean, P. (1995). Modelling the role of the cerebellar fastigial nuclei in producing accurate saccades: the
837 importance of burst timing. *Neuroscience* 68, 1059–1077
- 838 Dean, P., Mayhew, J. E., and Langdon, P. (1994). Learning and maintaining saccadic accuracy: a model of
839 brainstemcerebellar interactions. *Journal of Cognitive Neuroscience* 6, 117–138
- 840 Dean, P. and Porrill, J. (2008). Adaptive filter models of the cerebellum: computational analysis. *Cerebellum*
841 7, 567–571
- 842 Deubel, H. and Schneider, W. X. (1996). Saccade target selection and object recognition: Evidence for a
843 common attentional mechanism. *Vision Research* 36, 1827–1837. doi:10.1016/0042-6989(95)00294-4
- 844 DeWolf, T., Stewart, T. C., Slotine, J.-J., and Eliasmith, C. (2016). A spiking neural model of adaptive arm
845 control. *Proceedings of the Royal Society B: Biological Sciences* 283, 20162134. doi:10.1098/rspb.2016.
846 2134
- 847 Dorris, M. C., Par, M., and Munoz, D. P. (1997). Neuronal Activity in Monkey Superior Colliculus Related
848 to the Initiation of Saccadic Eye Movements. *The Journal of Neuroscience* 17, 8566
- 849 Edelman, J. A. and Keller, E. L. (1996). Activity of visuomotor burst neurons in the superior colliculus
850 accompanying express saccades. *Journal of Neurophysiology* 76, 908
- 851 Federighi, P., Cevenini, G., Dotti, M. T., Rosini, F., Pretegiani, E., Federico, A., et al. (2011). Differences
852 in saccade dynamics between spinocerebellar ataxia 2 and late-onset cerebellar ataxias. *Brain* 134,
853 879–891. doi:10.1093/brain/awr009
- 854 Fuchs, A. and Luschei, E. (1970). Firing patterns of abducens neurons of alert monkeys in relationship to
855 horizontal eye movement. *Journal of Neurophysiology* 33, 382–392
- 856 Galvan, A. and Wichmann, T. (2008). Pathophysiology of Parkinsonism. *Clinical Neurophysiology* 119,
857 1459–1474. doi:10.1016/j.clinph.2008.03.017
- 858 Gancarz, G. and Grossberg, S. (1998). A neural model of the saccade generator in the reticular formation.
859 *Neural Networks* 11, 1159–1174. doi:10.1016/S0893-6080(98)00096-3
- 860 Gian G. Mascetti and Jorge R. Arriagada (1981). Tectotectal interactions through the commissure of the
861 superior colliculi. An electrophysiological study. *Experimental Neurology* 71, 122–133
- 862 Girard, B. and Berthoz, A. (2005). From brainstem to cortex: Computational models of saccade generation
863 circuitry. *Progress in Neurobiology* 77, 215–251. doi:10.1016/j.pneurobio.2005.11.001

- 864 Gonon, F. (1997). Prolonged and extrasynaptic excitatory action of dopamine mediated by D1 receptors in
865 the rat striatum in vivo. *The Journal of neuroscience : the official journal of the Society for Neuroscience*
866 17, 5972–8
- 867 Goossens, H. (2006). Dynamic Ensemble Coding of Saccades in the Monkey Superior Colliculus. *Journal*
868 *of Neurophysiology* 95, 2326–2341. doi:10.1152/jn.00889.2005
- 869 Goossens, H. and Van Opstal, A. J. (2012). Optimal control of saccades by spatial-temporal activity
870 patterns in the monkey superior colliculus. *PLoS computational biology* 8, e1002508
- 871 Groh, J. M. (2001). Converting neural signals from place codes to rate codes. *Biological cybernetics* 85,
872 159–165
- 873 Groh, J. M. (2011). Effects of Initial Eye Position on Saccades Evoked by Microstimulation in the Primate
874 Superior Colliculus: Implications for Models of the SC Read-Out Process. *Frontiers in Integrative*
875 *Neuroscience* 4. doi:10.3389/fnint.2010.00130
- 876 Hallworth, N. E., Wilson, C. J., and Bevan, M. D. (2003). Apamin-sensitive small conductance calcium-
877 activated potassium channels, through their selective coupling to voltage-gated calcium channels, are
878 critical determinants of the precision, pace, and pattern of action potential generation in rat subthalamic
879 nucleus neurons in vitro. *The Journal of neuroscience* 23, 7525–7542
- 880 Harsing, L. G. and Zigmond, M. J. (1997). Influence of dopamine on GABA release in striatum: evidence
881 for D1-D2 interactions and non-synaptic influences. *Neuroscience* 77, 419–29
- 882 Hazy, T. E., Frank, M. J., and O'Reilly, R. C. (2007). Towards an executive without a homunculus:
883 computational models of the prefrontal cortex/basal ganglia system. *Philosophical Transactions of the*
884 *Royal Society B: Biological Sciences* 362, 1601–1613. doi:10.1098/rstb.2007.2055
- 885 Hepp, K. and Henn, V. (1983). Spatio-temporal recoding of rapid eye movement signals in the monkey
886 paramedian pontine reticular formation (PPRF). *Experimental brain research* 52, 105–120
- 887 Hepp, K., Van Opstal, A. J., Straumann, D., Hess, B. J., and Henn, V. (1993). Monkey superior colliculus
888 represents rapid eye movements in a two-dimensional motor map. *Journal of neurophysiology* 69,
889 965–979
- 890 Howard, L. A. and Tipper, S. (1997). Hand deviations away from visual cues: indirect evidence for
891 inhibition. *Experimental brain research* 113, 144–152
- 892 INCF Task Force on Multi-Scale Modeling (2011). Network Interchange for Neuroscience Modeling
893 Language (NineML)
- 894 Isa, T. (2002). Intrinsic processing in the mammalian superior colliculus. *Current Opinion in Neurobiology*
895 12, 668–677. doi:10.1016/S0959-4388(02)00387-2
- 896 Isa, T. and Hall, W. C. (2009). Exploring the Superior Colliculus In Vitro. *Journal of Neurophysiology*
897 102, 2581–2593. doi:10.1152/jn.00498.2009
- 898 James, S., Bell, O. A., Nazli, M. A. M., Pearce, R. E., Spencer, J., Tyrrell, K., et al. (2017). Target-distractor
899 synchrony affects performance in a novel motor task for studying action selection. *PLOS ONE* 12,
900 e0176945. doi:10.1371/journal.pone.0176945
- 901 Kleine, J. F. (2003). Saccade-Related Neurons in the Primate Fastigial Nucleus: What Do They Encode?
902 *Journal of Neurophysiology* 90, 3137–3154. doi:10.1152/jn.00021.2003
- 903 Khn, A. A., Williams, D., Kupsch, A., Limousin, P., Hariz, M., Schneider, G.-H., et al. (2004). Event-
904 related beta desynchronization in human subthalamic nucleus correlates with motor performance. *Brain*
905 : a journal of neurology 127, 735–46. doi:10.1093/brain/awh106
- 906 Lefvre, P., Quaia, C., and Optican, L. M. (1998). Distributed model of control of saccades by superior
907 colliculus and cerebellum. *Neural Networks* 11, 1175–1190
- 908 Linden, R. and Perry, V. (1983). Massive retinotectal projection in rats. *Brain research* 272, 145–149

- 909 Ling, L., Fuchs, A. F., Siebold, C., and Dean, P. (2007). Effects of initial eye position on saccade-related
910 behavior of abducens nucleus neurons in the primate. *Journal of Neurophysiology* 98, 3581–3599
- 911 Marcos, E. and Genovesio, A. (2016). Determining Monkey Free Choice Long before the Choice Is Made:
912 The Principal Role of Prefrontal Neurons Involved in Both Decision and Motor Processes. *Frontiers in*
913 *Neural Circuits* 10. doi:10.3389/fncir.2016.00075
- 914 Marino, R. A., Trappenberg, T. P., Dorris, M., and Munoz, D. P. (2012). Spatial Interactions in the Superior
915 Colliculus Predict Saccade Behavior in a Neural Field Model. *Journal of Cognitive Neuroscience* 24,
916 315–336. doi:10.1162/jocn_a_00139
- 917 McCarthy, M. M., Moore-Kochlacs, C., Gu, X., Boyden, E. S., Han, X., and Kopell, N. (2011). Striatal
918 origin of the pathologic beta oscillations in Parkinson’s disease. *Proceedings of the National Academy*
919 *of Sciences* 108, 11620–11625. doi:10.1073/pnas.1107748108
- 920 McIlwain, J. T. (1982). Lateral spread of neural excitation during microstimulation in intermediate gray
921 layer of cat’s superior colliculus. *Journal of Neurophysiology* 47, 167–178
- 922 McPeek, R. M. (2006). Incomplete Suppression of Distractor-Related Activity in the Frontal Eye Field
923 Results in Curved Saccades. *Journal of Neurophysiology* 96, 2699–2711. doi:10.1152/jn.00564.2006
- 924 McPeek, R. M., Han, J. H., and Keller, E. L. (2003). Competition Between Saccade Goals in the Superior
925 Colliculus Produces Saccade Curvature. *Journal of Neurophysiology* 89, 2577–2590. doi:10.1152/jn.
926 00657.2002
- 927 McPeek, R. M. and Keller, E. L. (2002). Saccade Target Selection in the Superior Colliculus During a
928 Visual Search Task. *Journal of Neurophysiology* 88, 2019–2034
- 929 Meredith, M. A. and Ramoa, A. S. (1998). Intrinsic Circuitry of the Superior Colliculus: Pharmacophysio-
930 logical Identification of Horizontally Oriented Inhibitory Interneurons. *Journal of Neurophysiology* 79,
931 1597–1602
- 932 Mitchinson, B., Chan, T.-S., Chambers, J., Pearson, M., Humphries, M., Fox, C., et al. (2010). BRAHMS:
933 Novel middleware for integrated systems computation. *Advanced Engineering Informatics* 24, 49–61.
934 doi:10.1016/j.aei.2009.08.002
- 935 Mitchinson, B. and James, S. S. (2015). BRAHMS. RRID: SCR_015642
- 936 Morn, J., Shibata, T., and Doya, K. (2013). The Mechanism of Saccade Motor Pattern Generation
937 Investigated by a Large-Scale Spiking Neuron Model of the Superior Colliculus. *PLoS ONE* 8, e57134.
938 doi:10.1371/journal.pone.0057134
- 939 Munoz, D. P. (2002). Commentary: Saccadic eye movements: overview of neural circuitry. In *Progress in*
940 *Brain Research*, ed. D. M. J. Hyona, W. Heide and R. Radach (Elsevier), vol. Volume 140. 89–96
- 941 Nambu, A., Yoshida, S.-i., and Jinnai, K. (1990). Discharge patterns of pallidal neurons with input from
942 various cortical areas during movement in the monkey. *Brain Research* 519, 183–191. doi:10.1016/
943 0006-8993(90)90076-N
- 944 N’Guyen, S., Thurat, C., and Girard, B. (2014). Saccade learning with concurrent cortical and subcortical
945 basal ganglia loops. *Frontiers in Computational Neuroscience* 8. doi:10.3389/fncom.2014.00048
- 946 Nowotny, T. (2011). Flexible neuronal network simulation framework using code generation for NVidia
947 CUDA. *BMC Neuroscience* 12, P239. doi:10.1186/1471-2202-12-S1-P239
- 948 Nowotny, T., Cope, A. J., Yavuz, E., Stimberg, M., Goodman, D. F., Marshall, J., et al. (2014). SpineML
949 and Brian 2.0 interfaces for using GPU enhanced Neuronal Networks (GeNN). *BMC Neuroscience* 15,
950 P148. doi:10.1186/1471-2202-15-S1-P148
- 951 Olivier, E., Corvisier, J., Pauluis, Q., and Hardy, O. (2000). Evidence for glutamatergic tectotectal neurons
952 in the cat superior colliculus: a comparison with GABAergic tectotectal neurons. *European Journal of*
953 *Neuroscience* 12, 2354–2366

- 954 Ottes, F. P., Van Gisbergen, J. A., and Eggermont, J. J. (1986). Visuomotor fields of the superior colliculus:
955 A quantitative model. *Vision Research* 26, 857–873. doi:10.1016/0042-6989(86)90144-6
- 956 Papapavlou, C. and Moustakas, K. (2014). Physics-based modelling and animation of saccadic eye
957 movement
- 958 Quaia, C., Lefvre, P., and Optican, L. M. (1999). Model of the Control of Saccades by Superior Colliculus
959 and Cerebellum. *Journal of Neurophysiology* 82, 999
- 960 Quaia, C., Par, M., Wurtz, R. H., and Optican, L. M. (2000). Extent of compensation for varia-
961 tions in monkey saccadic eye movements. *Experimental Brain Research* 132, 39–51. doi:10.1007/
962 s002219900324
- 963 Reppert, T. R., Lempert, K. M., Glimcher, P. W., and Shadmehr, R. (2015). Modulation of Saccade
964 Vigor during Value-Based Decision Making. *Journal of Neuroscience* 35, 15369–15378. doi:10.1523/
965 JNEUROSCI.2621-15.2015
- 966 Richmond, P. (2015). DAMSON
- 967 Richmond, P., Cope, A., Gurney, K., and Allerton, D. J. (2014). From Model Specification to Simulation
968 of Biologically Constrained Networks of Spiking Neurons. *Neuroinformatics* 12, 307–323. doi:10.1007/
969 s12021-013-9208-z
- 970 Robinson, D. (1972). Eye movements evoked by collicular stimulation in the alert monkey. *Vision Research*
971 12, 1795–1808. doi:10.1016/0042-6989(72)90070-3
- 972 Robinson, D. A. (1975). Oculomotor control signals. In *Basic mechanisms of ocular motility and their*
973 *clinical implications*, eds. G. Lennerstrand and P. Bach-y Rita (Oxford: Pergamon). 337–374
- 974 Rovamo, J. and Virsu, V. (1979). An estimation and application of the human cortical magnification factor.
975 *Experimental Brain Research* 37, 495–510. doi:10.1007/BF00236819
- 976 Schall, J. D. and Thompson, K. G. (1999). Neural selection and control of visually guided eye movements.
977 *Annual review of neuroscience* 22, 241–259
- 978 Schiller, P. H., Sandell, J. H., and Maunsell, J. H. (1987). The effect of frontal eye field and superior
979 colliculus lesions on saccadic latencies in the rhesus monkey. *Journal of Neurophysiology* 57, 1033
- 980 Schwartz, E. L. (1977). Spatial mapping in the primate sensory projection: Analytic structure and relevance
981 to perception. *Biological Cybernetics* 25, 181–194. doi:10.1007/BF01885636
- 982 Schwartz, E. L. (1980). Computational anatomy and functional architecture of striate cortex: A spatial
983 mapping approach to perceptual coding. *Vision Res.* 20, 645–669
- 984 Schweighofer, N., Arbib, M. A., and Dominey, P. F. (1996). A model of the cerebellum in adaptive control
985 of saccadic gain. *Biological Cybernetics* 75, 19–28
- 986 Scudder, C. A. (1988). A new local feedback model of the saccadic burst generator. *J Neurophysiol* 59,
987 1454
- 988 Seth, A., Sherman, M., Reinbolt, J. a., and Delp, S. L. (2011). OpenSim: a musculoskeletal modeling
989 and simulation framework for in silico investigations and exchange. *Procedia IUTAM* 2, 212–232.
990 doi:10.1016/j.piutam.2011.04.021
- 991 Slotnick, S. D., Klein, S. A., Carney, T., and Sutter, E. E. (2001). Electrophysiological estimate of human
992 cortical magnification. *Clinical Neurophysiology* 112, 1349–1356
- 993 Sparks, D. L. (2002). The brainstem control of saccadic eye movements. *Nature Reviews Neuroscience* 3,
994 952–964. doi:10.1038/nrn986
- 995 Sparks, D. L. and Nelson, I. S. (1987). Sensory and motor maps in the mammalian superior colliculus.
996 *Trends in Neurosciences* 10, 312–317. doi:10.1016/0166-2236(87)90085-3

- 997 Stanton, G. B., Goldberg, M. E., and Bruce, C. J. (1988a). Frontal eye field efferents in the macaque
998 monkey: I. Subcortical pathways and topography of striatal and thalamic terminal fields. *Journal of*
999 *Comparative Neurology* 271, 473–492. doi:10.1002/cne.902710402
- 1000 Stanton, G. B., Goldberg, M. E., and Bruce, C. J. (1988b). Frontal eye field efferents in the macaque
1001 monkey: II. Topography of terminal fields in midbrain and pons. *The Journal of Comparative Neurology*
1002 271, 493–506. doi:10.1002/cne.902710403
- 1003 Sterling, P. (1971). Receptive fields and synaptic organization of the superficial gray layer of the cat
1004 superior colliculus. *Vision Research* 11, 309–IN47. doi:10.1016/0042-6989(71)90048-4
- 1005 Tabareau, N., Bennequin, D., Berthoz, A., Slotine, J.-J., and Girard, B. (2007). Geometry of the superior
1006 colliculus mapping and efficient oculomotor computation. *Biological cybernetics* 97, 279–292
- 1007 Takagi, M., Zee, D. S., and Tamargo, R. J. (1998). Effects of Lesions of the Oculomotor Vermis on Eye
1008 Movements in Primate: Saccades. *Journal of Neurophysiology* 80, 1911
- 1009 Talbot, S. and Marshall, W. (1941). Physiological Studies on Neural Mechanisms of Visual Localization
1010 and Discrimination*. *American Journal of Ophthalmology* 24, 1255–1264. doi:10.1016/S0002-9394(41)
1011 91363-6
- 1012 Thurat, C., NGuyen, S., and Girard, B. (2015). Biomimetic race model of the loop between the superior
1013 colliculus and the basal ganglia: Subcortical selection of saccade targets. *Neural Networks* 67, 54–73.
1014 doi:10.1016/j.neunet.2015.02.004
- 1015 Tipper, S. P., Howard, L. A., and Paul, M. A. (2001). Reaching affects saccade trajectories. *Experimental*
1016 *Brain Research* 136, 241–249
- 1017 Van Gisbergen, J., Van Opstal, A., and Tax, A. (1987). Collicular ensemble coding of saccades based on
1018 vector summation. *Neuroscience* 21, 541–555. doi:10.1016/0306-4522(87)90140-0
- 1019 Van Gisbergen, J. A. M., Van Opstal, A. J., and Schoenmakers, J. J. M. (1985). Experimental test of two
1020 models for the generation of oblique saccades. *Experimental brain research* 57, 321–336
- 1021 Van Opstal, A. J. and Goossens, H. H. L. M. (2008). Linear ensemble-coding in midbrain superior colliculus
1022 specifies the saccade kinematics. *Biological Cybernetics* 98, 561–577. doi:10.1007/s00422-008-0219-z
- 1023 Van Opstal, A. J., Hepp, K., Hess, B. J., Straumann, D., and Henn, V. (1991). Two-rather than three-
1024 dimensional representation of saccades in monkey superior colliculus. *Science* 252, 1313–1315
- 1025 Vokoun, C. R., Huang, X., Jackson, M. B., and Basso, M. A. (2014). Response Normalization in the
1026 Superficial Layers of the Superior Colliculus as a Possible Mechanism for Saccadic Averaging. *Journal*
1027 *of Neuroscience* 34, 7976–7987. doi:10.1523/JNEUROSCI.3022-13.2014
- 1028 Vokoun, C. R., Jackson, M. B., and Basso, M. A. (2010). Intralaminar and Interlaminar Activity within the
1029 Rodent Superior Colliculus Visualized with Voltage Imaging. *Journal of Neuroscience* 30, 10667–10682.
1030 doi:10.1523/JNEUROSCI.1387-10.2010
- 1031 Vokoun, C. R., Jackson, M. B., and Basso, M. A. (2011). Circuit dynamics of the superior colliculus
1032 revealed by in vitro voltage imaging: Vokoun et al. *Annals of the New York Academy of Sciences* 1233,
1033 41–47. doi:10.1111/j.1749-6632.2011.06166.x
- 1034 Waitzman, D. M., Ma, T. P., Optican, L. M., and Wurtz, R. H. (1991). Superior colliculus neurons mediate
1035 the dynamic characteristics of saccades. *Journal of Neurophysiology* 66, 1716–1737
- 1036 Walker, R., Deubel, H., Schneider, W. X., and Findlay, J. M. (1997). Effect of remote distractors on saccade
1037 programming: evidence for an extended fixation zone. *Journal of neurophysiology* 78, 1108–1119
- 1038 Wilson, C. J. (2004). A Model of Reverse Spike Frequency Adaptation and Repetitive Firing of Subthalamic
1039 Nucleus Neurons. *Journal of Neurophysiology* 91, 1963–1980. doi:10.1152/jn.00924.2003

- 1040 Wu, H. H., Williams, C. V., and McLoon, S. C. (1994). Involvement of nitric oxide in the elimination
 1041 of a transient retinotectal projection in development. *SCIENCE-NEW YORK THEN WASHINGTON-*,
 1042 1593–1593
- 1043 Wurtz, R. H. and Goldberg, M. E. (1972). Activity of superior colliculus in behaving monkey. III. Cells
 1044 discharging before eye movements. *J Neurophysiol* 35, 575–586

FIGURES

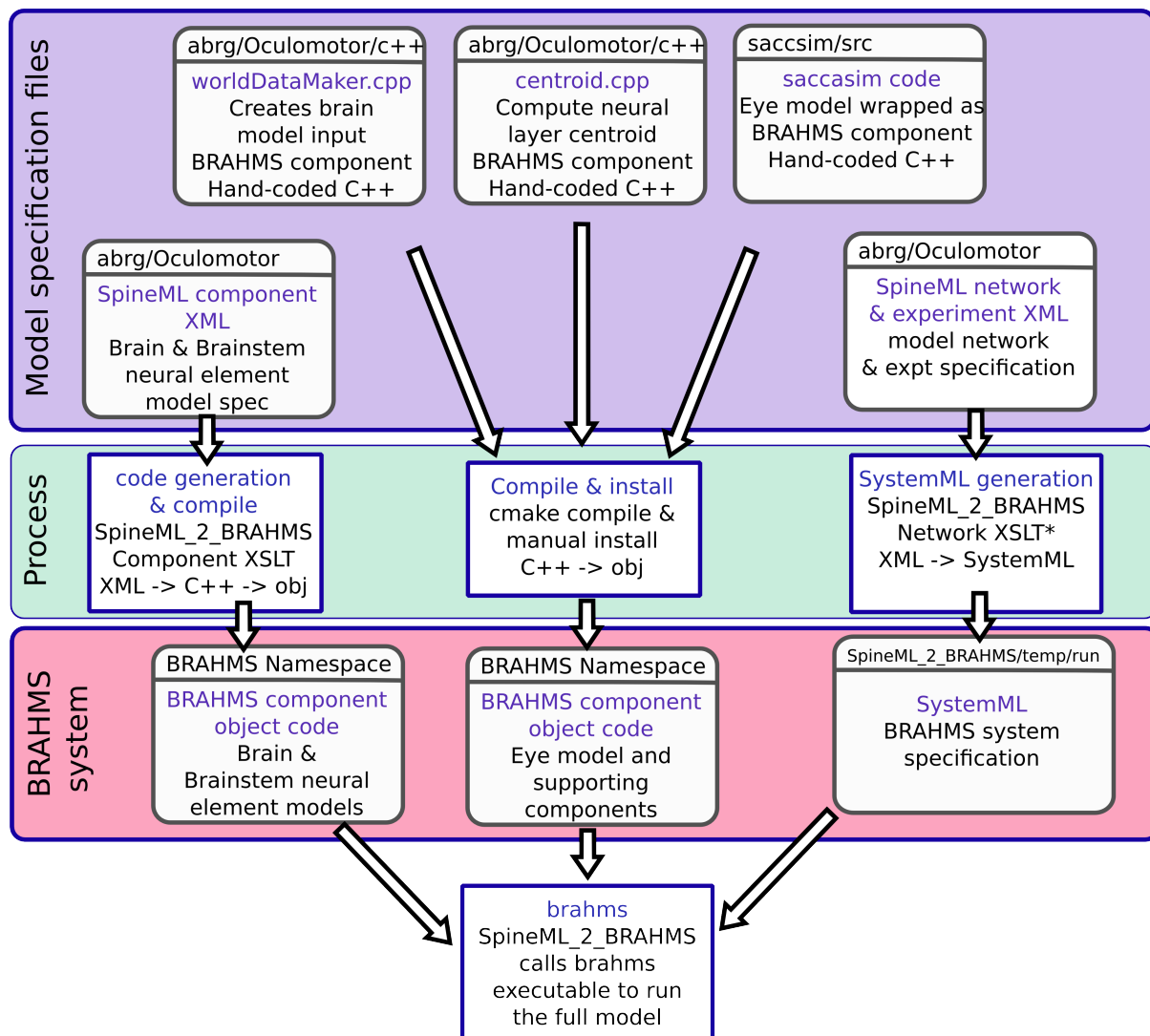


Figure 1. The model framework. The model is specified using a combination of declarative XML files and hand-coded C++. These original model specifications are shown within the blue box. b) The green box shows the processes which are applied to the model specification to produce the BRAHMS system. Most of the process is defined within the scripts which make up SpineML_2_BRAHMS, but the hand-written components must be manually compiled and installed within the BRAHMS Namespace, allowing the BRAHMS executable to locate them at runtime. c) The red box shows the resulting BRAHMS system ready to be executed by the BRAHMS executable. In practice, this call is made by SpineML_2_BRAHMS.

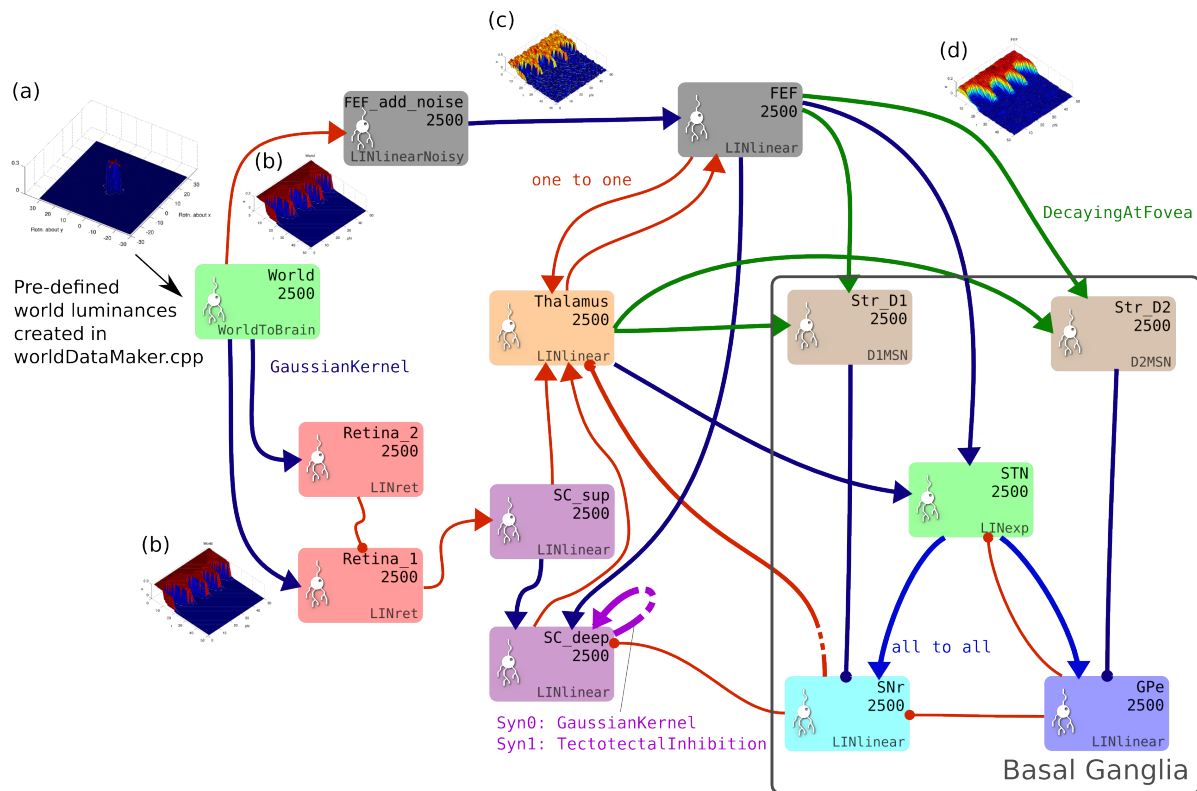


Figure 2. The brain model. This is the SpineCreator ‘network layer’ view of the model. Each box represents a neural population with 2500 elements, arranged in a 50×50 grid. The SpineML component name is printed on the bottom right corner of each population box and the population name is at the top. The overall connectivity between populations is represented by the projection arrows with the colour indicating the connectivity scheme (one-to-one connections are red, Gaussian kernel connections are dark blue and so on). Excitatory connections have arrowheads and inhibitory connections have circles, although for details of the behaviour of the connections, the weight-update and post-synapse components must be studied. Briefly, the model comprises a *World* population, into which a retinotopically organised view of the world is introduced. This information is passed into cortical populations (FEF) and subcortical populations (SC) via a simple model of the retina. These feed a cortico-thalamo-basal ganglia loop, which selects which region of the deep layer of superior colliculus should be disinhibited, allowing activity to build up therein. The five populations comprising the basal ganglia are enclosed in a grey outline. Note that substantia nigra pars compacta is not modelled here, instead the level of dopamine in the striatum is set via a parameter in the Str.D1 and Str.D2 populations

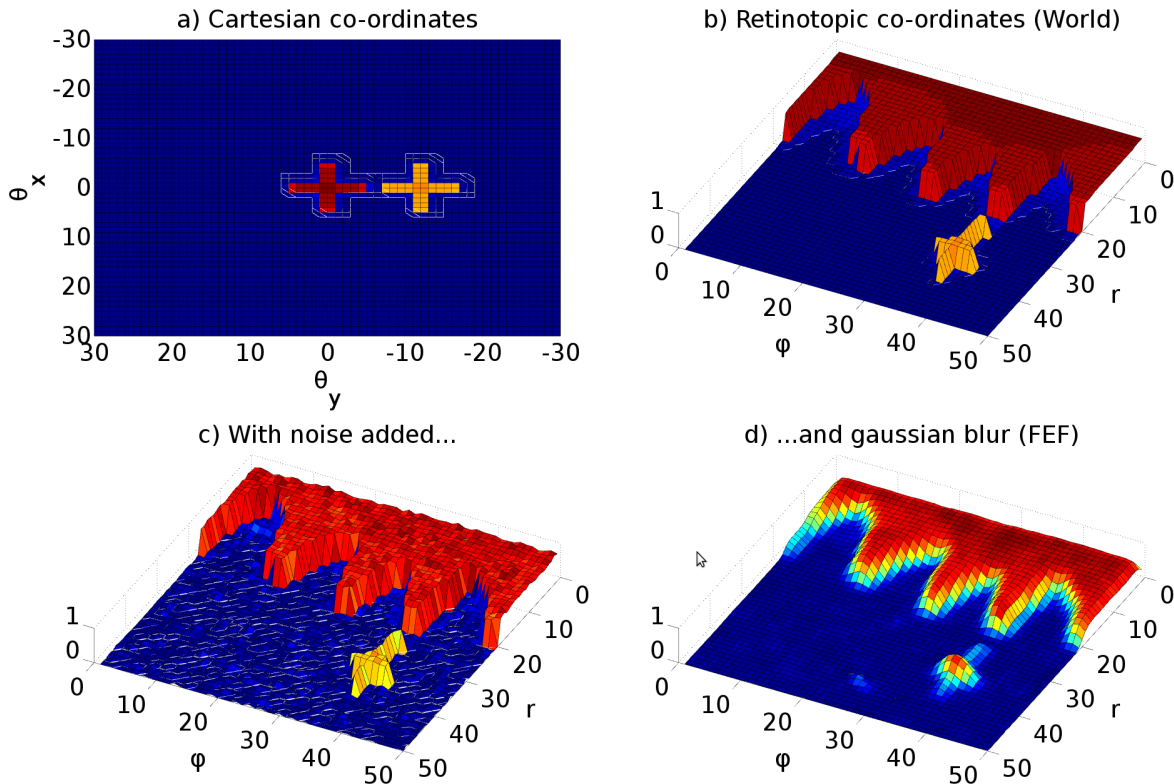


Figure 3. Representative mapping from eye's frame of reference in Cartesian co-ordinates to retinotopic co-ordinates. (a) The mapping of luminances in the eye's frame of reference. The world input is pre-defined by a JSON configuration file. Luminance position, size and shape can be defined in this file, along with the times at which luminances appear and disappear. The worldDataMaker.cpp code computes the locations of the luminances in the eye's frame of reference, given its rotational state. It also computes a 2D Gaussian convolution of the luminances. Here, there are two cross shaped luminances spanning 10° , one of value 0.8 at the fixation point (0,0) and one of value 0.5 at a peripheral position (0,- 12°). Note that these crosses have the same 'bar width' of 2° as the crosses used in the simulations, but their span of 10° is greater than the 6° used in the simulations, to make these images clearer. (b) The locations of the luminances in the eye's frame of reference are then converted into retinotopic co-ordinates, with centrally located luminances being represented at low values of r and more peripheral luminances having higher values of r . ϕ encodes rotational angle: 1 and 50 encode upward movement; 13 is left; 25 is down; 37 is right. The output of the World component is fed into FEF_add_noise and into the retinal neuron populations. The colour map makes it possible to distinguish between the two crosses. (c) The FEF_add_noise populations adds a level of noise to the signal representing processing of the signal in visual cortex. (d) A Gaussian projection from FEF_add_noise to FEF further blurs the activity in FEF. FEF is the input to the basal ganglia and one input to superior colliculus.

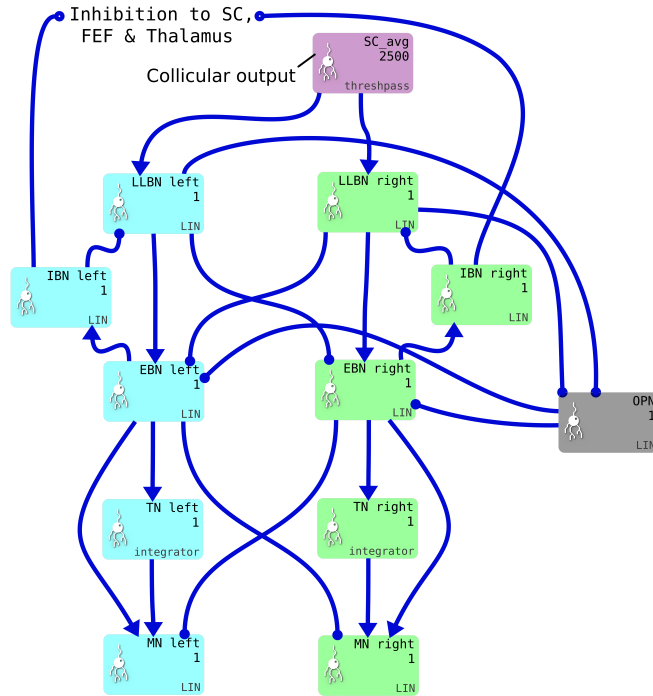


Figure 4. One pair of channels of the saccadic burst generator (SBG) for left (cyan) or right (green) movements. Collicular activity in SC_avg excites the channels via SBG weight maps. Each box represents a neural population and shows the population name, the number of neural elements (here 2500 or 1) and the SpineML component name; LIN for Leaky integrator or *integrator*. Key: LLBN: Long lead burst neurons; IBN: Inhibitory burst neurons; OPN: Omnipause neurons; EBN: Excitatory burst neurons; TN: Tonic neurons; MN: Motoneurons.

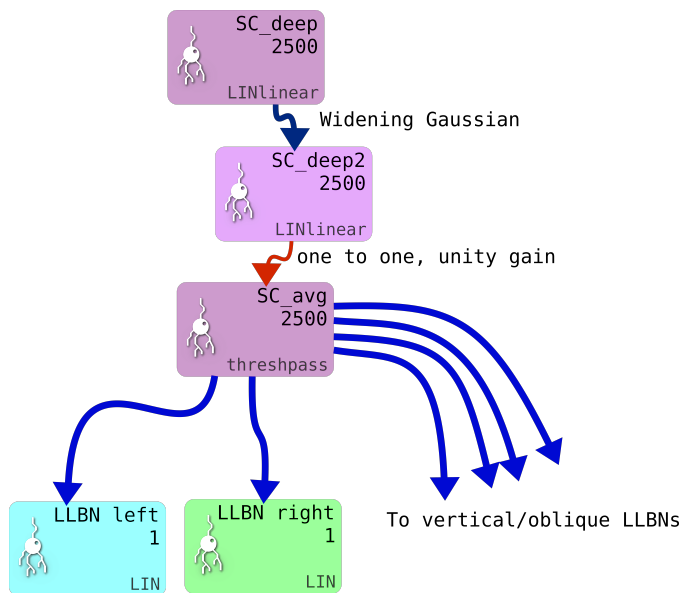


Figure 5. Showing the additional deep layer of superior colliculus (SC_deep2) and the output layer (SC_avg, named for the fact that in an earlier version of the model, it received the output of the centroid of SC_deep). The widening Gaussian projection is shown as the arrow between SC_deep and SC_deep2.

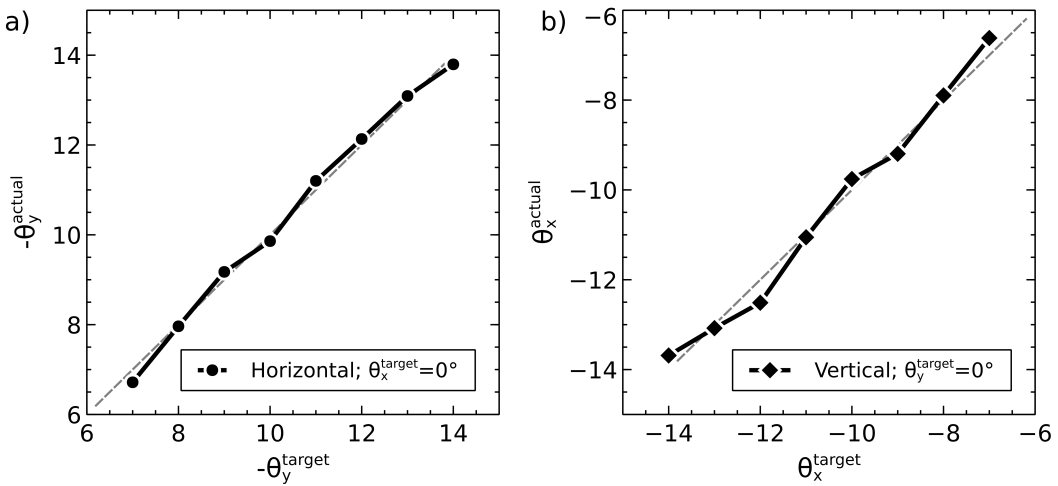


Figure 6. Accuracy at different target eccentricities for fixation luminance 0.2 and target luminance 0.3.

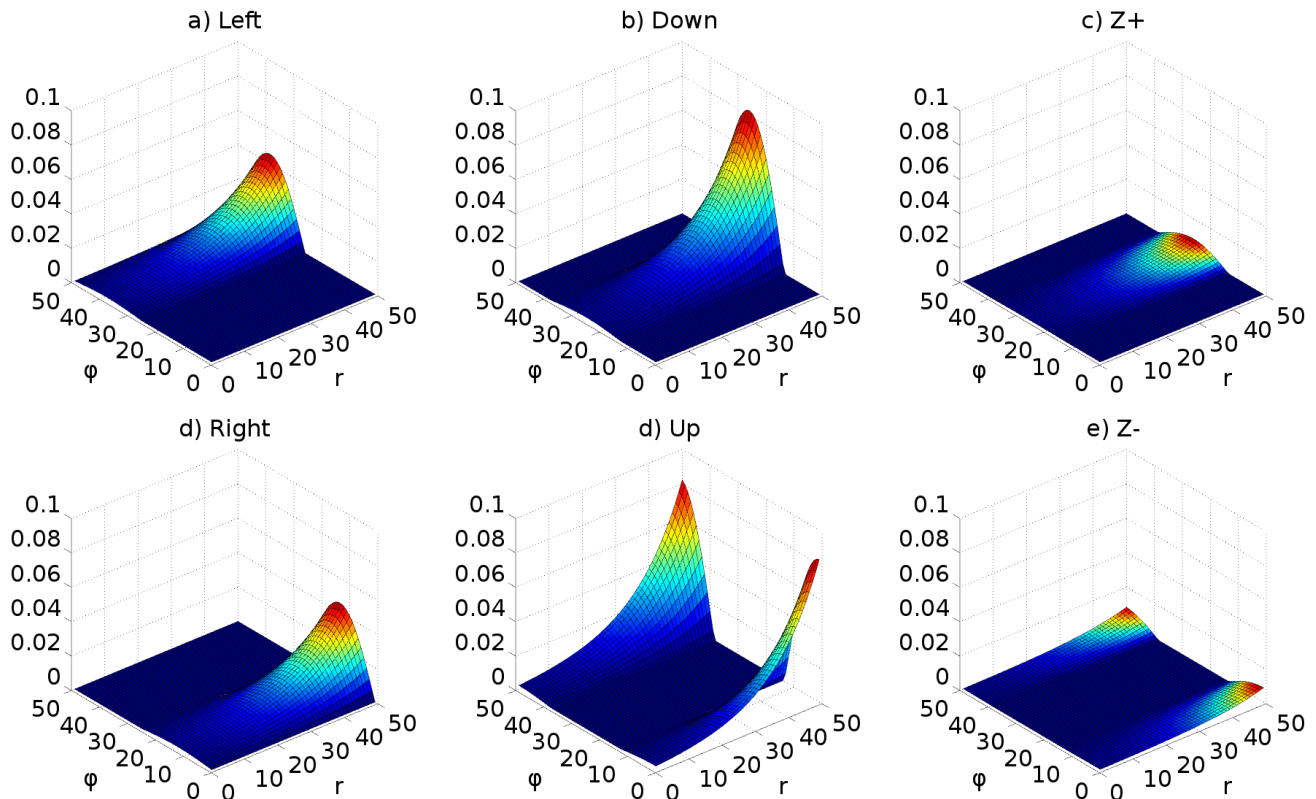


Figure 7. Weight maps for the connections between the output layer of superior colliculus and the six long lead burst neurons of the saccadic burst generator model. Each map increases exponentially with increasing r , multiplied by $\cosine(\phi)$ about its ‘active’ axis. **Check whether Left & Right are wrong way round**

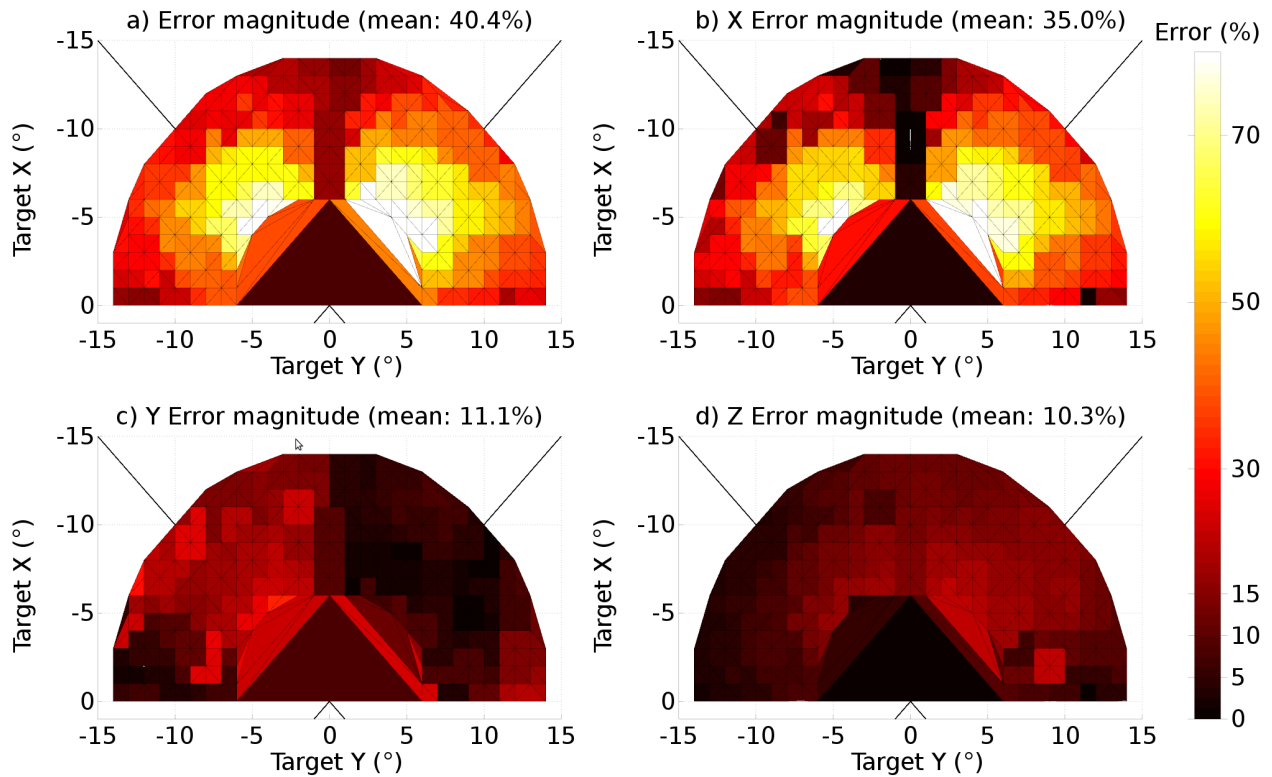


Figure 8. The end-point error surface for the original, naïve model (TModel3). a) The ratio of the magnitudes of the total error vector and the target vector, expressed as a percentage. b) The ratio of the magnitude of the x component of the error vector to the magnitude of the target vector, expressed as a percentage. c) As (b) but for the y component. d) As (b), for z component. All colour maps are shown with the same scale. The target rotations, θ_x^t and θ_y^t are denoted ‘Target X’ and ‘Target Y’ in the figure.

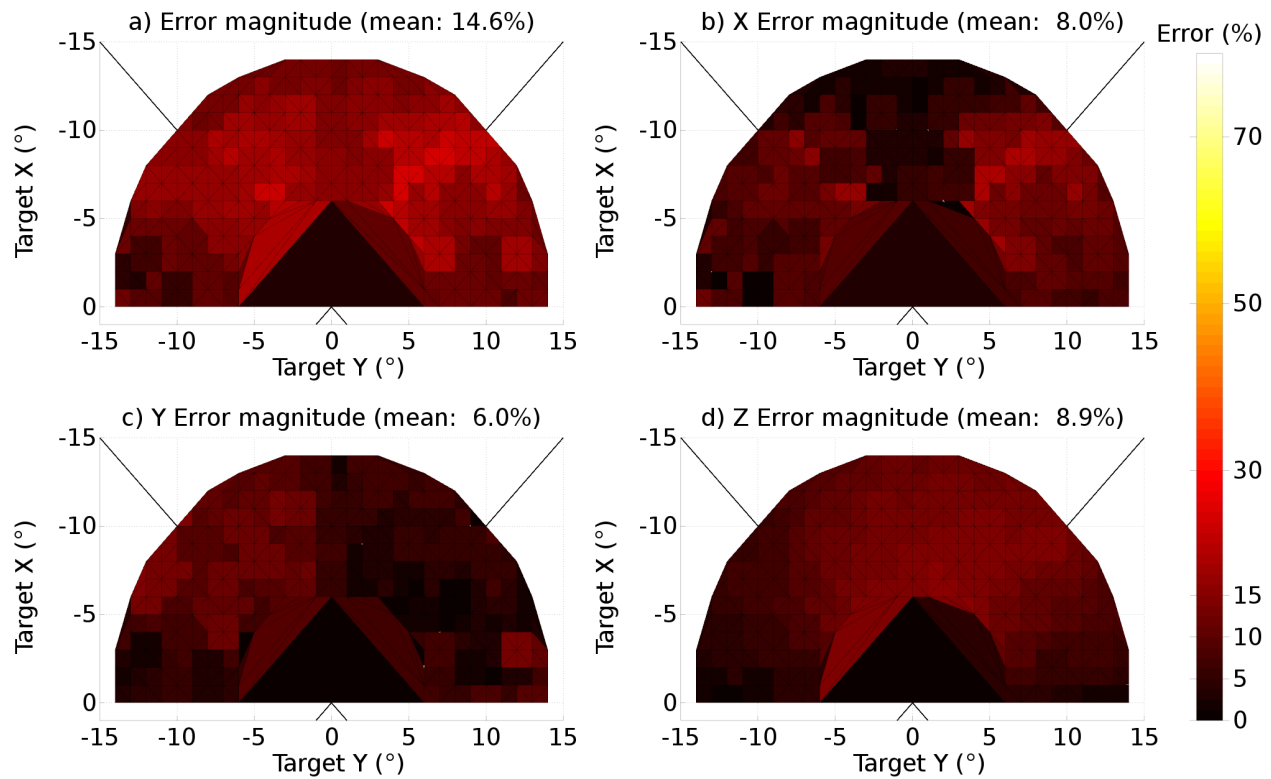


Figure 9. The end-point error surface for the model in which a widening projection field was added to the model of the superior colliculus. a) The ratio of the magnitudes of the total error vector and the target vector, expressed as a percentage. b) The ratio of the magnitude of the x component of the error vector to the magnitude of the target vector, expressed as a percentage. c) As (b) but for the y component. d) As (b), for z component. All colour maps are shown with the same scale. The target rotations, θ_x^t and θ_y^t are denoted ‘Target X’ and ‘Target Y’ in the figure. Note that the range of the colour scale is 0 to 20%, a much smaller range than the range in Fig 8.

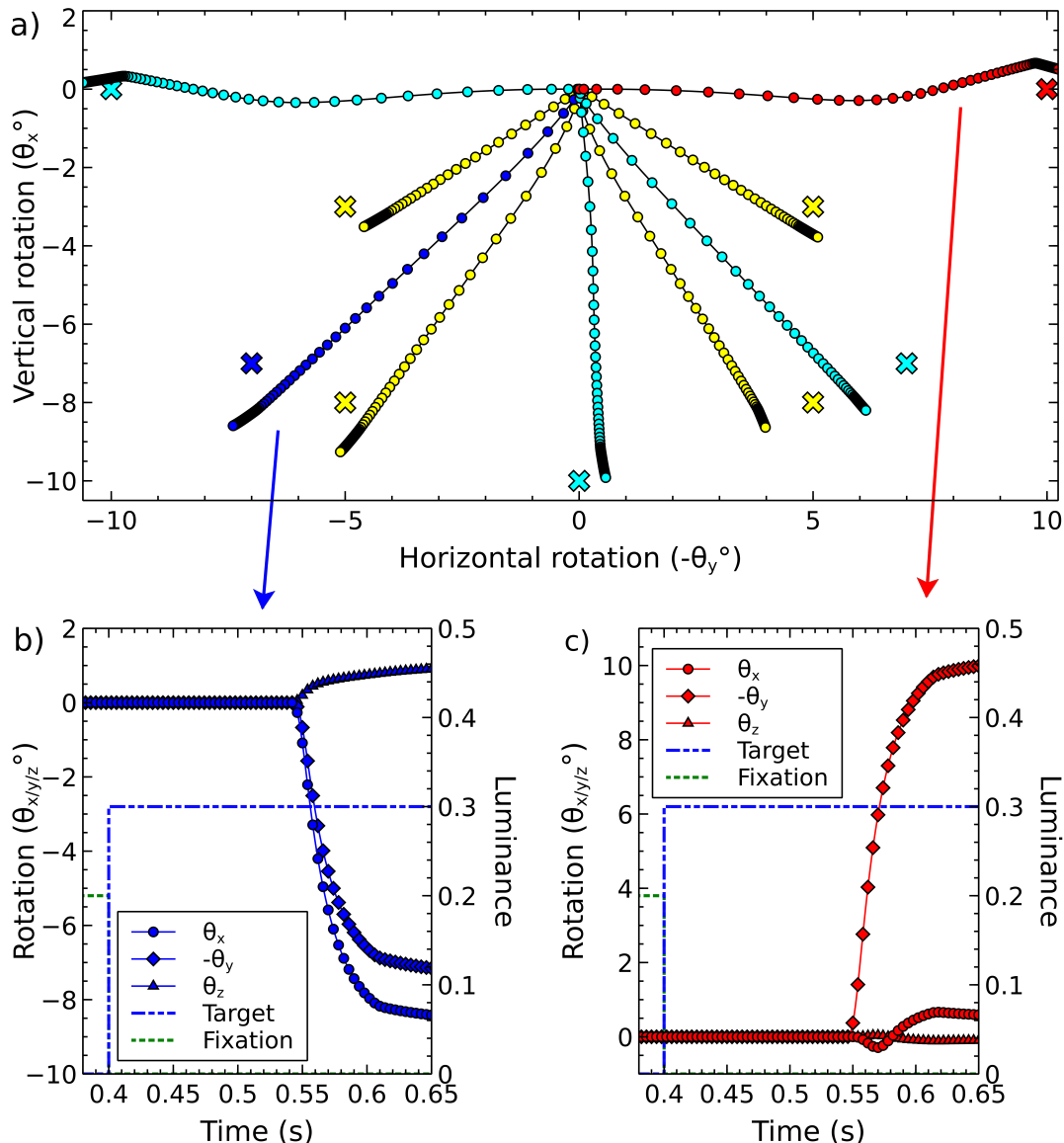


Figure 10. Representative single saccades. a) Trajectories from 9 saccades to a single target at 9 different locations. In each case, a fixation cross luminance of magnitude 0.2 was displayed at (0,0), the start position of the eye, until time 0.4 s. The target luminance, magnitude 0.3 was illuminated at time 0.4 s. Trajectory shape is dependent on the target position, and there is a variable amount of error in the end-points achieved by the model. Colour is used in this diagram as an aid to distinguishing different saccades and their targets; for a given saccade, the target location is given by the cross of the same colour closest to the end of the trajectory. b) The three rotational components of the ‘blue’ saccade, to target location (-7,-7). c) The three rotational components of the ‘red’ saccade, to target location (0,-10).

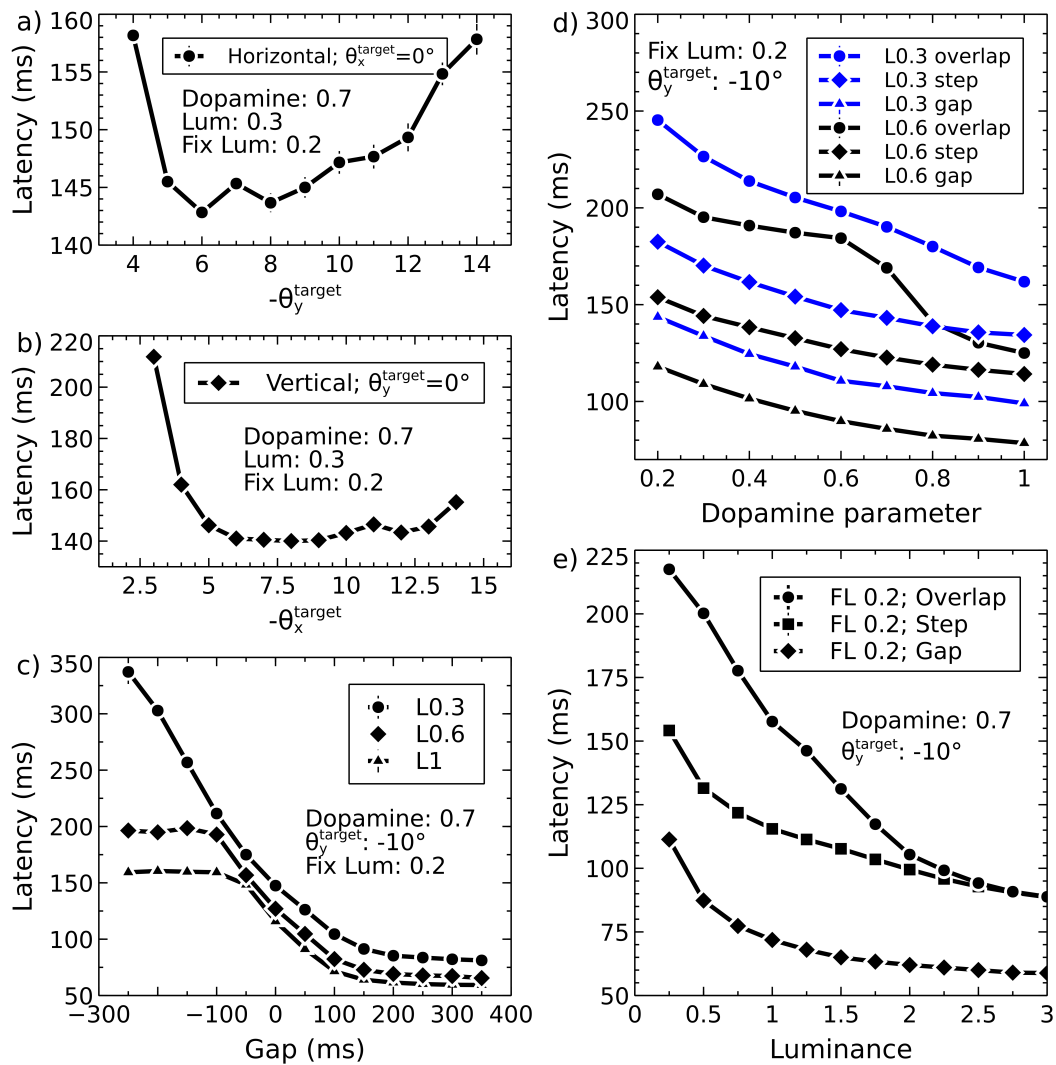


Figure 11. Exploring saccade latencies. a) Latency to first movement as a function of target eccentricity for horizontal targets. b) Latency vs. eccentricity for vertical targets. c) Latency vs. gap at three different luminance values. d) The effect of the dopamine parameter on saccade latencies in gap, step and overlap conditions, for two different target luminances. e) Saccade vs. luminance showing gradual transition between reflexive and express behaviour.

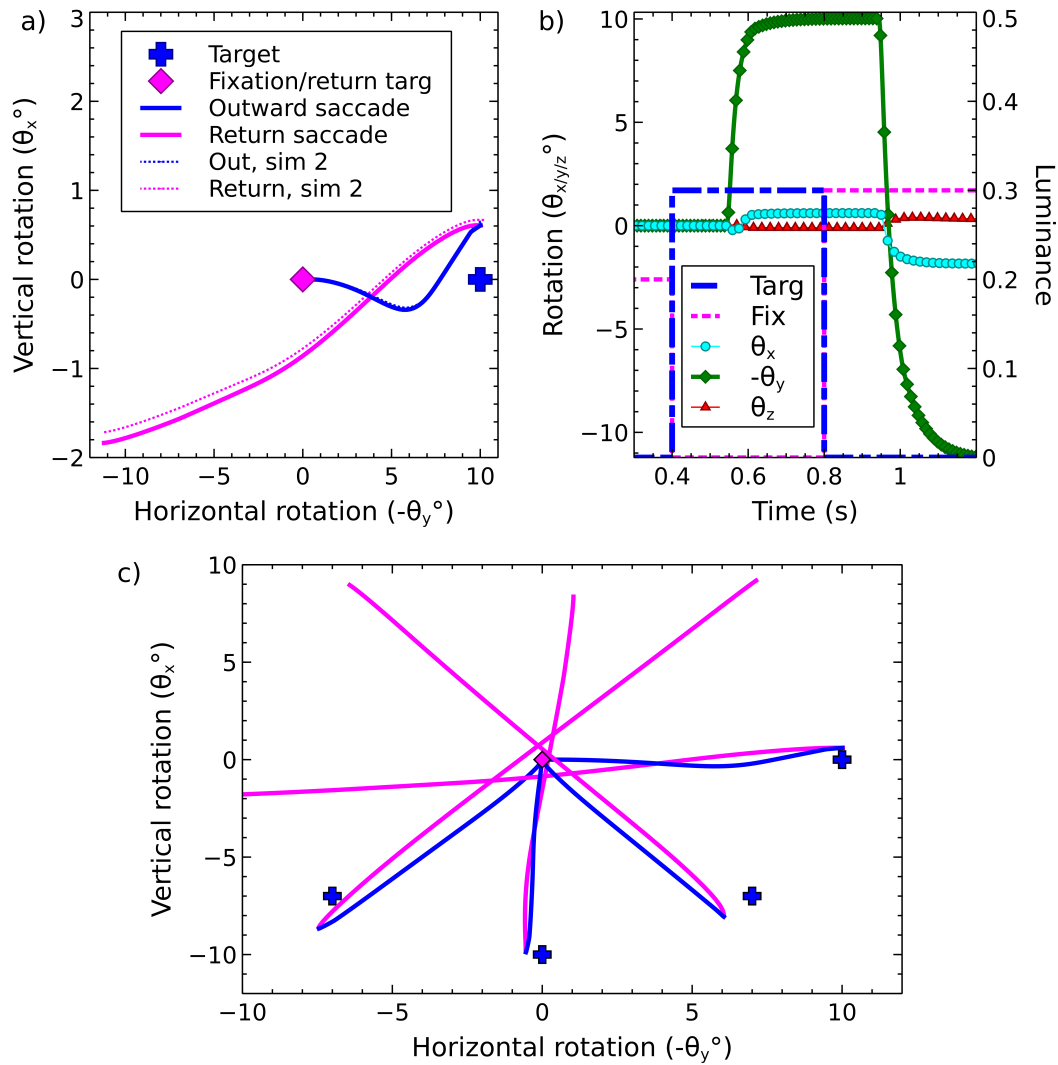


Figure 12. There and back - a saccade to a target, followed by return to the original fixation. a) Out and return saccade to a target at (0, -10°) b) Rotational components of the saccade shown in (a). c) Outward and return trajectories for the saccade shown in (a) alongside saccades to three other targets.

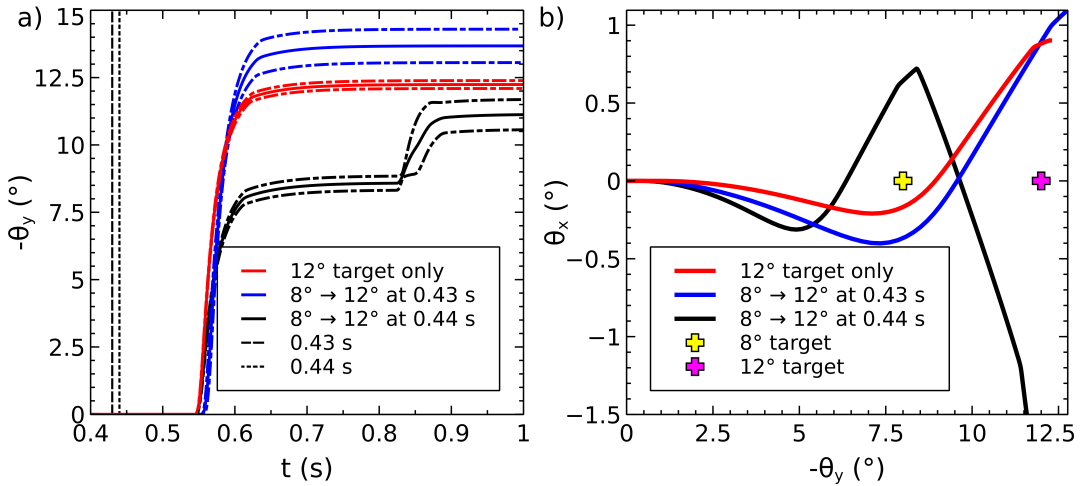


Figure 13. Double steps. The effect of illuminating a first target at 8° or 12° , followed by a second target at 12° or 8° . a) Horizontal rotation of the eye plotted vs. time for a saccade to the 12° target only (red), and to an 8° target at 0.4 s followed by a 12° target after 30 ms (blue) or 40 ms (black). The timings are indicated by vertical lines. When the second target is presented up to 30 ms after the initial target, the initial target has not had time to dominate the output saccade and a saccade to a location close to the second target is made. If the delay is 40 ms or more, the activity from the initial target has time to cause a built up of activity in SC_deep and an initial saccade close to the first target is made, followed, after a longer than usual latency period, with a second saccade closer to the second target. In this graph, the mean of five separate simulations is plotted along with ± 1 standard deviation around the mean. b) The θ_x/θ_y trajectories corresponding to the data presented in (a).